Zhu *et al. Geochem Trans* (2021) 22:1
https://doi.org/10.1186/s12932-021-00075-1

Geochemical Transactions

RESEARCH ARTICLE Open Access

Dissolution and solubility of calcite-rhodochrosite solid solutions [$(Ca_{1-x}Mn_x)CO_3$] at 25 °C

Yinian Zhu[1*], Peijie Nong[1], Nan Mo[1], Zongqiang Zhu[2,3*], Huan Deng[1], Shen Tang[2], Hongqu Yang[1], Lihao Zhang[2] and Xingxing Wang[1]

Abstract

A complete series of calcite-rhodochrosite solid solutions [$(Ca_{1-x}Mn_x)CO_3$] are prepared, and their dissolution processes in various water samples are experimentally investigated. The crystal morphologies of the solid solutions vary from blocky spherical crystal aggregates to smaller spheres with an increasing incorporation of Mn in the solids. Regarding dissolution in N_2-degassed water, air-saturated water and CO_2-saturated water at 25 °C, the aqueous Ca and Mn concentrations reach their highest values after 1240–2400 h, 6–12 h and < 1 h, respectively, and then decrease gradually to a steady state; additionally, the ion activity products (log_IAP) at the final steady state (≈ solubility products in log_K_{sp}) are estimated to be -8.46 ± 0.06, -8.44 ± 0.10 and -8.59 ± 0.10 for calcite [$CaCO_3$], respectively, and -10.25 ± 0.08, -10.26 ± 0.10 and -10.28 ± 0.03, for rhodochrosite [$MnCO_3$], respectively. As X_{Mn} increases, the log_IAP values decrease from $-8.44 \sim -8.59$ for calcite to $-10.25 \sim -10.28$ for rhodochrosite. The aqueous Mn concentrations increase with an increasing Mn/(Ca + Mn) molar ratio (X_{Mn}) of the $(Ca_{1-x}Mn_x)CO_3$ solid solutions, while the aqueous Ca concentrations show the highest values at $X_{Mn} = 0.53–0.63$. In the constructed Lippmann diagram of subregular $(Ca_{1-x}Mn_x)CO_3$ solid solutions, the solids dissolve incongruently, and the data points of the aqueous solutions move progressively up to the Lippmann *solutus* curve and then along the *solutus* curve or saturation curve of pure $MnCO_3$ to the Mn-poor side. The microcrystalline cores of the spherical crystal aggregates are preferentially dissolved to form core hollows while simultaneously precipitating Mn-rich hexagonal prisms.

Keywords: Calcite, Rhodochrosite, Solid solution, Dissolution, Solubility, Lippmann diagram

Introduction

Manganese (II) is a toxic divalent metal that can be found in excessive amounts in various water bodies, soils and rocks [1, 2]. Its mobility in the natural environment is controlled by various geochemical processes, including its incorporation into carbonates to form rhombohedral calcite-rhodochrosite solid solutions [(Ca,Mn)CO_3] via a dissolution–recrystallization process [3–6]. Furthermore, the precipitation of solid (Ca, Mn)CO_3 solutions can be a potential technique to eliminate Mn(II) from wastewater [7]. The study of these solid solutions is therefore valuable to understand the Mn cycle in the environment [8].

Although the ionic radius of Ca^{2+} is approximately 20% larger than that of Mn^{2+}, Mn can substitute Ca in the calcite lattice [9]. While the (Ca, Mn)CO_3-H_2O system has been broadly investigated in the literature, several essential problems remain unresolved, and many contradictory results have been reported [2]. A limited rhombohedral calcite-rhodochrosite solid solution with a wide miscibility gap can be formed at low temperatures [10,

*Correspondence: zhuyinian@glut.edu.cn; zhuzongqiang@glut.edu.cn
[1] College of Environmental Science and Engineering, Guilin University of Technology, Guilin 541004, China
[2] Guangxi Key Laboratory of Environmental Pollution Control Theory and Technology, Guilin University of Technology, Guilin 541004, China
Full list of author information is available at the end of the article

11]. Conversely, natural calcian rhodochrosite and manganoan calcite have been reported to have a complete component range between calcite and rhodochrosite [4, 12], and a nearly continuous series between $CaCO_3$ and $MnCO_3$ can be prepared in the laboratory [6, 13].

Despite the importance of authigenic mixed Mn–Ca–Mg carbonates in the geochemical cycle of Mn on the Earth's surface, very limited studies have been conducted to determine the solubility products and stability domain of (Ca,Mn)CO_3 solid solutions [4, 6]. The accurate determination of the thermodynamic solubilities of carbonate minerals at low temperatures is therefore essential to the interpretation of the behavior of these minerals in natural waters. Fewer studies have been conducted on solid solutions than on single-component carbonates. Many inconsistent solubility values for $MnCO_3$ can be found in the literature. The Gibbs energies of formation (ΔG_f°) of $MnCO_3$ range from −809.89 kJ/mol to −818.81 kJ/mol with solubility products (log_K_{sp}) from −9.43 to −10.99 [5, 14]. Generally, synthetic solids yield lower ΔG_f° values and appear to be more soluble than natural solids [5]. In addition, the estimation of the dimensionless Guggenheim coefficient a_0 for the (Ca,Mn)CO_3 solid solutions at low temperature differs greatly. The rhombohedral (Ca,Mn)CO_3 solid solutions as a complete series has $a_0 < 2$ (25 °C) [15, 16]. Whereas $a_0 = +3.23$ (25 °C) is theoretically calculated [10] and $a_0 = -1 \pm 3$ (20 °C) is derived from the experimental stoichiometric solubilities of synthetic Mn-calcite [$Ca_{0.75}Mn_{0.25}CO_3$] [17]. From the phase relationships in anoxic marine muds, a_0 is estimated to be −3.5 (5 °C) [18], which is nearly equal to the a_0 value of −4 (20 °C) for synthetic Mn-calcite [$Ca_{0.86}Mn_{0.14}CO_3$] [13]. The lack of agreement among (Ca,Mn)CO_3 solid solutions make it difficult to put forward reliable geochemical models [11].

The dissolution behaviors of the synthesized $Ca_{0.75}Mn_{0.25}CO_3$, $Ca_{0.52}Mn_{0.48}CO_3$ and $Ca_{0.25}Mn_{0.75}CO_3$ in CO_2-saturated water at 20 °C were studied experimentally, and the dissolution paths were analyzed with respect to the stoichiometric saturation and thermodynamic equilibrium using a Lippmann diagram, showing that the metastable solids equilibrated with aqueous solution through dissolution/crystallization at ambient temperature [4]. During the precipitation of the complete $(Ca_{1-x}Mn_x)CO_3$ solid solutions, no Ca^{2+} and Mn^{2+} fractionation between the solid and water was detected at a very high precipitation rate, whereas the Mn^{2+} cations were commonly enriched in the solid phase at a lower precipitation rate [13]. However, the exact formation and stability conditions of rhodochrosite-calcite solid solutions on a mechanistic and quantitative basis are still not fully understood [19]. During the dissolution of four $(Ca_{1-x}Mn_x)CO_3$ solids (x = 0–0.12) in acidic solutions, the aqueous Mn^{2+} concentrations first increased and then decreased with the formation of rhodochrosite ($MnCO_3$), indicating that the dissolution/precipitation of carbonates might be impacted by impurities in calcite [20]. The synthetic disordered Ca-Mg-rhodochrosite $(Mn_{0.58}Ca_{0.39}Mg_{0.03})CO_3$ dissolved congruently in water at 25 °C, from which the ion activity product (log_IAP) of −10.39 was extrapolated [6]. In brief, information about the thermodynamic data of $(Ca_{1-x}Mn_x)CO_3$ solid solutions is still deficient, although their dissolution/precipitation can exert a significant effect on Mn cycling in the environment.

Therefore, the present work aims to determine the apparent solubility of $CaCO_3$–$MnCO_3$ solid solutions illustrating some detail of the dissolution process. Firstly, calcite-rhodochrosite solid solutions [$(Ca_{1-x}Mn_x)CO_3$] with varying Mn/(Ca + Mn) molar ratios (X_{Mn}) from 0.00 to 1.00 are precipitated and characterized. Then, the dissolution process of the obtained solid samples and the release of the components (Mn^{2+}, Ca^{2+}, CO_3^{2-}/HCO_3^-) are experimentally studied by batch tests. Finally, a Lippmann diagram for the $(Ca_{1-x}Mn_x)CO_3$ solid solutions is constructed to examine the interaction in the solid solution–aqueous solution (SS-AS) system to evaluate the solubility of Mn-carbonates and the Mn distribution in aqueous environments.

Experimental methods

Solid synthesis

Eleven crystal solids (CR-00–CR-10) of the $(Ca_{1-x}Mn_x)CO_3$ solid solutions were precipitated by mixing a 2 M Ca + Mn solution with a 0.5 M NH_4HCO_3 solution based on following equation: $M^{2+} + CO_3^{2-} = MCO_3$, where M = (Ca + Mn) (Table 1). Analytical reagent grade chemicals and ultrapure water were used. The solids were prepared at room temperature (22 ± 1 °C) by the dropwise addition of 50 mL of a 2 M mixed solution of $Ca(NO_3)_2$ and $Mn(NO_3)_2$ with different Mn/(Ca + Mn) molar ratios into 1000 mL of a vigorously agitated 0.5 M NH_4HCO_3 solution in N_2 gas (Table 1). The resulting suspensions were then stirred for another 10 min. Finally, the precipitates were separated from the solutions by membrane filtration, washed cautiously with ethanol and dried for 24 h at 90 °C.

Characterization

The components of the obtained solids were estimated by wet chemical analyses, i.e., 10 mg of each solid was decomposed in 20 mL of 1 M nitric acid solution that was then diluted to 100 mL with ultrapure water. The total calcium and manganese contents were determined using inductively coupled plasma-optical emission spectrometry (ICP-OES, Perkin-Elmer Optima 7000DV). All

Table 1 Summary of the synthesis and composition of calcite-rhodochrosite solid solutions [$(Ca_{1-x}Mn_x)CO_3$]

Sample No	Volume of the precursors (mL)			Mn/(Ca + Mn) molar ratio (x)					
	2 M $Ca(NO_3)_2$	2 M $Mn(NO_3)_2$	0.5 M NH_4HCO_3	Starting solution	Synthetic solid[a]	Synthetic solid[b]	After 300d dissolution in water[b]		
							Air-saturated	N_2-degassed	CO_2-Saturated
CR-00	50	0	1000	0.00	0.00	0.00	0.00	0.00	0.00
CR-01	45	5	1000	0.10	0.11	0.07	0.12	0.12	0.12
CR-02	40	10	1000	0.20	0.22	0.17	0.24	0.24	0.24
CR-03	35	15	1000	0.30	0.32	0.25	0.35	0.34	0.35
CR-04	30	20	1000	0.40	0.42	0.34	0.46	0.45	0.45
CR-05	25	25	1000	0.50	0.53	0.43	0.56	0.55	0.56
CR-06	20	30	1000	0.60	0.63	0.62	0.66	0.65	0.65
CR-07	15	35	1000	0.70	0.72	0.73	0.74	0.73	0.75
CR-08	10	40	1000	0.80	0.83	0.84	0.84	0.84	0.84
CR-09	5	45	1000	0.90	0.92	0.92	0.93	0.92	0.93
CR-10	0	50	1000	1.00	1.00	1.00	1.00	1.00	1.00

[a] Chemical analysis; [b]EDS analysis

solids were identified crystallographically by comparing their X-ray diffraction (XRD, X'Pert PRO, PANalytical B.V.) patterns with a Cu Kα radiation source at 40 kV and 40 mA to the reference codes 01-081-2027 for calcite and 00-044-1472 for rhodochrosite of the International Center for Diffraction Data (ICDD). Field-emission scanning electron microscopy (FE-SEM, JEOL JEM-7800F) was applied to examine the morphological images of the precipitates and their approximate sizes. The solids were also embedded in resins, polished until their grains had been sectioned and then coated using carbon to study the compositional inhomogeneity and zoning phenomena within the crystals by backscattered electron imaging (BSEI) with the FE-SEM instrument.

Dissolution experiments

Dissolution experiments of the $(Ca_{1-x}Mn_x)CO_3$ solid solutions in a closed system were performed. The working principle of the closed-system was described in detail previously [6]. Instrumental-grade N_2, air and CO_2 were used to saturate the initial solutions. Briefly, 5 g of the $(Ca_{1-x}Mn_x)CO_3$ solid solutions were weighed and added into three groups of labeled 100 mL polyethylene terephthalate (PET) bottles, and 100 mL of N_2-degassed, air-saturated and CO_2-saturated ultrapure water was then used to fill the bottles. After being capped, the bottles were immersed in water baths at 25 °C. At various intervals (1, 3, 6, 12, 24, 48, 72, 120, 240, 360, 480, 720, 960, 1200, 1440, 1680, 1920, 2160, 2400, 4800 and 7200 h) after the start of the experiment, one bottle from each group was removed. The pH values were immediately measured, and the solutions were filtered with 0.45 μm membrane filters. The HCO_3^-/CO_3^{2-} concentrations were measured by using an automatic potentiometric titrator (888 Titrando, Metrohm, Switzerland). Additionally, 5 mL of the solutions was filtered through 0.22 μm membranes and acidified in 25 mL flasks using 0.2% nitric acid. The total calcium and manganese contents were determined using ICP-OES. At the experimental end, the solid residuals were collected from the bottles, washed with ethanol, dried at 90 °C for 24 h, and characterized using XRD and FE-SEM as previously described.

Thermodynamic calculations

For the dissolution of the $(Ca_{1-x}Mn_x)CO_3$ solid solutions, the activities of free Mn^{2+}, Ca^{2+} and CO_3^{2-} were first estimated using the geochemical code PHREEQC (Version 3.6.2) [21], and then the ion activity products (IAPs) were calculated after the definitions, which equaled the solubility products (K_{sp}) of the $(Ca_{1-x}Mn_x)CO_3$ solid solutions at equilibrium. The component species involved in the simulation contained Mn^{2+}, $MnOH^+$, $Mn(OH)_2^0$, $Mn(OH)_3^-$, $Mn(OH)_4^{2-}$ and $MnHCO_3^+$ for manganese; Ca^{2+}, $CaOH^+$, $CaHCO_3^+$ and $CaCO_3^0$ for calcium; and CO_3^{2-}, HCO_3^-, $H_2CO_3^0$, $CaHCO_3^+$ and $MnHCO_3^+$ for carbonate. The built-in database minteq.v4.dat of PHREEQC included the thermodynamic properties of all solid phases and aqueous species for modeling (Additional file 1: Appendix S1). The ionic strength values (< 0.01166 mol/L) lay in the applicable range for the extended Debye-Hückel equation.

Results and discussion

Solid characterization

Composition

The compositions of the obtained solids were close to the Mn/(Ca + Mn) mole ratios of the starting solution

(Table 1). The predicted Mn/(Ca + Mn) molar ratios (X_{Mn}) were not linearly correlated with the measured X_{Mn}, showing the preferential Mn uptake of the solids [5]. After the dissolution of the $(Ca_{1-x}Mn_x)CO_3$ solid solutions in the N_2-degassed, air-saturated and CO_2-saturated water samples for 300 d, the Mn/(Ca + Mn) molar ratios (X_{Mn}) of the residual solids increased slightly, indicating the preferential retention of Mn in the solids.

XRD

The synthesized crystals belonged to calcite–rhodochrosite $[(Ca_{1-x}Mn_x)CO_3]$ solid solutions, and all XRD spectra were confirmed to be the $R\,\overline{3}\,c$ space group (Fig. 1). The crystals of $X_{Mn} = 0$ and 1 (CR-00 and CR-10) were identical to calcite (ICSD Reference code 01-072-1937) and rhodochrosite (00-044-1472), respectively. The reflection peaks, particularly (104), shifted slightly to higher angles with increased Mn incorporation, owing to the smaller interplanar distance of Mn-calcite in comparison with pure calcite. All well-crystallized solids differed only in the peak locations, widths and intensities in their XRD spectra, indicating that they were not simple mixtures of the calcite and rhodochrosite endmembers but rather calcite–rhodochrosite $[(Ca_{1-x}Mn_x)CO_3]$ solid solutions (Fig. 1; Additional file 1: Appendix S2-A).

Regarding the solids that were formed from aqueous solutions with low Mn^{2+}/Ca^{2+} ratios (CR-00 and CR-01) or high Mn^{2+}/Ca^{2+} ratios (CR-07–CR-10), only the peaks corresponding to the calcite or rhodochrosite endmembers were found in the XRD patterns (Fig. 1). Regarding the solids that were formed from aqueous solutions with intermediate Mn^{2+}/Ca^{2+} ratios (CR-02–CR-06), all the XRD patterns exhibited double peaks, and as a result, two groups of reflections were considered for indexing: in the first group, the 2θ angles were close to the corresponding reflections of calcite and lower than the second group whose reflections were closer to the rhodochrosite peaks. The presence of double peaks indicated compositional heterogeneities in the samples, which was also confirmed in the electron microscopy observations and microprobe analyses. As the Mn^{2+}/Ca^{2+} ratios in the starting solutions increased, the reflections assigned to the Mn-rich zones became progressively more intense [2].

Additional reflections that could be attributed to ordered kutnohorite were not found in any of the XRD patterns [22]. After dissolution for 300 d, no obvious variations, including additional peaks for portlandite $[Ca(OH)_2]$ and pyrochroite $[Mn(OH)_2]$, were found for all solids (Fig. 1; Additional file 1: Appendix S2-B).

SEM

The morphologies of the crystals exhibited a strong dependence on the Mn concentrations in the starting solutions. A variety of crystal morphologies were

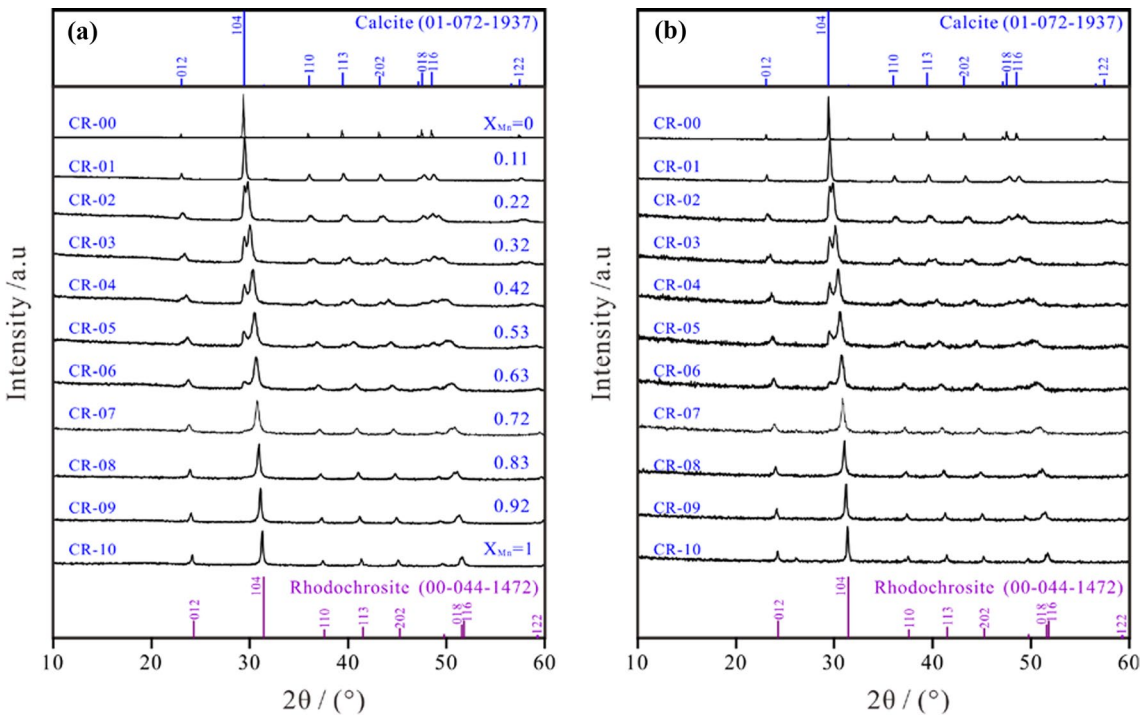

Fig. 1 Diffraction patterns of the $(Ca_{1-x}Mn_x)CO_3$ solid solutions (**a**) before and (**b**) after dissolution in air-saturated water for 300 d

obtained, showing the effects of Mn^{2+} (even at low concentrations) on the growth of the {104} faces of calcite [2, 11].

The synthesized calcite (CR-00) showed a typical morphology with rhombohedral habits defined by {104} planes with a grain size of ~ 10 μm (Fig. 2; Additional file 1: Appendix S3). The sizes of the $(Ca_{1-x}Mn_x)CO_3$ solid solutions decreased with an increasing X_{Mn}, although the morphologies remained rhombohedral for the $(Ca_{1-x}Mn_x)CO_3$ aggregations (Fig. 2), showing that manganese could influence the growth and morphology of calcite [11, 20]. As the Mn concentrations increased, the $(Ca_{1-x}Mn_x)CO_3$ solid solutions varied from blocky crystals to spherulites and peanut-like aggregates [23]. The crystal morphologies of the intermediate compositions and the $MnCO_3$ endmember (X_{Mn} = 0.11–1.00; CR-01–CR-10) varied from blocky spherical crystal aggregates to smaller spheres following the change in the Mn contents of the initial solutions (Fig. 2). The individual was a crystal, the surface of which was formed by the aggregation of numerous minuscule blocks of {104} facets that appeared slightly disoriented, as they traced the external shape of a solid that could be considered spherical. This final morphology was a result of intense splitting phenomena during the growth process [2].

The increase in the relative amounts of Mn in the starting solution could cause a further modification of the external morphology of the crystals (Fig. 2; Additional file 1: Appendix S3). With increasing Mn concentrations, the size of the individual crystals decreased, and the terrace texture of the external morphology was eliminated and replaced by a very smooth and rounded surface. This morphological modification was also accompanied by a decrease in the 'physical' spherical particle diameters. This decrease in crystal sizes was expected due to the lower solubilities of Mn-rich carbonates in comparison to Ca-rich carbonates, i.e., the less soluble Mn-rich phases were more metastable; consequently, they crystallized at a higher supersaturation [24]. This higher supersaturation caused a larger nucleation density, consequently decreasing the crystal size. Similar results have also been observed in earlier studies [2, 23].

Sections of the crystal aggregates (CR-01–CR-10) grown from starting aqueous solutions containing Mn^{2+} showed clear oscillatory concentric zoning, which indicated the core-to-rim compositional heterogeneity of the bulk crystal spheres (Figs. 3 and 4; Additional file 1: Appendix S4 and S5) or the core-to-rim crystalline heterogeneity of the pure $MnCO_3$ spheres (CR-10) (Fig. 5). Since variations in image brightness represented changes in composition, the visibility of compositional zoning could be attained by the backscattered imaging of polished central sections of crystals. Backscattered electron images of some representative individuals (CR-03 and CR-05) together with the corresponding compositional profiles are shown in Fig. 3 before dissolution and in Additional file 1: Appendix S4 after dissolution. The central part of the crystal was always relatively rich in Mn. Surrounding this core were successive Ca-rich and Mn-rich rings [2]. The thickness of these zones ranged from approximately 0.8 μm, and variations within a ring never exceeded an X_{Mn} value of 0.10. In the outer part, the morphology of an initial rhombohedron could still be seen (Additional file 1: Appendix S5).

High compositional gradients of crystals have been proven to be a major characteristic of solid solutions with a great difference in the solubilities of the endmembers (2 to 3 orders of magnitude) [25, 26] and could be easy to explain considering changes in the fluid composition during crystal growth [2, 27, 28]. The Mn-rich phases of the $(Ca,Mn)CO_3$ solid solutions were clearly much less soluble (~ 2 orders of magnitude) than the Ca-rich phases, so Mn was preferentially incorporated in the solid phases at the primary nucleation stage. The consumption of Mn in the bulk crystals caused the local depletion of Mn^{2+} in the solutions and the subsequent growth of Ca-rich solid phases. The Ca incorporation in the crystal reduced the Ca concentrations in the nucleation area, and Mn once again started to be preferentially incorporated toward the solids. Because of the large difference in the solubilities of calcite and rhodochrosite, a very small change in the solution composition during Mn enrichment or depletion could cause a large compositional gradient in the growing solid [2].

Generally, all solids after dissolution showed the same macroscopic characteristics as before, i.e., the endmember calcite (CR-00) had a common appearance with rhombohedral habits, and the morphologies of crystals of the intermediate compositions and the endmember rhodochrosite (CR-01–CR-10) changed from blocky spherical crystal aggregates to spheres following the increase in Mn content (Fig. 2; Additional file 1: Appendix S3).

After calcite dissolution, the edges of the crystals degenerated, and etch pits on the surface were observed (Additional file 1: Appendix S3). Furthermore, it was observed that the microcrystalline cores of the spherical crystal aggregates (CR-01–CR-10) were preferentially dissolved to form hollows while simultaneously precipitating Mn-rich hexagonal prisms (Figs. 4 and 5; Additional file 1: Appendix S5). The rhombohedral crystals were not fully closed so solution could flow into the core of the sphere, which resulted in the first dissolution of the core crystals that had a smaller grain size than the peripheral crystals. Needle-like crystals or hexagonal prisms without rhombohedral terminations more clearly formed with an increasing dissolution time and Mn/(Ca + Mn)

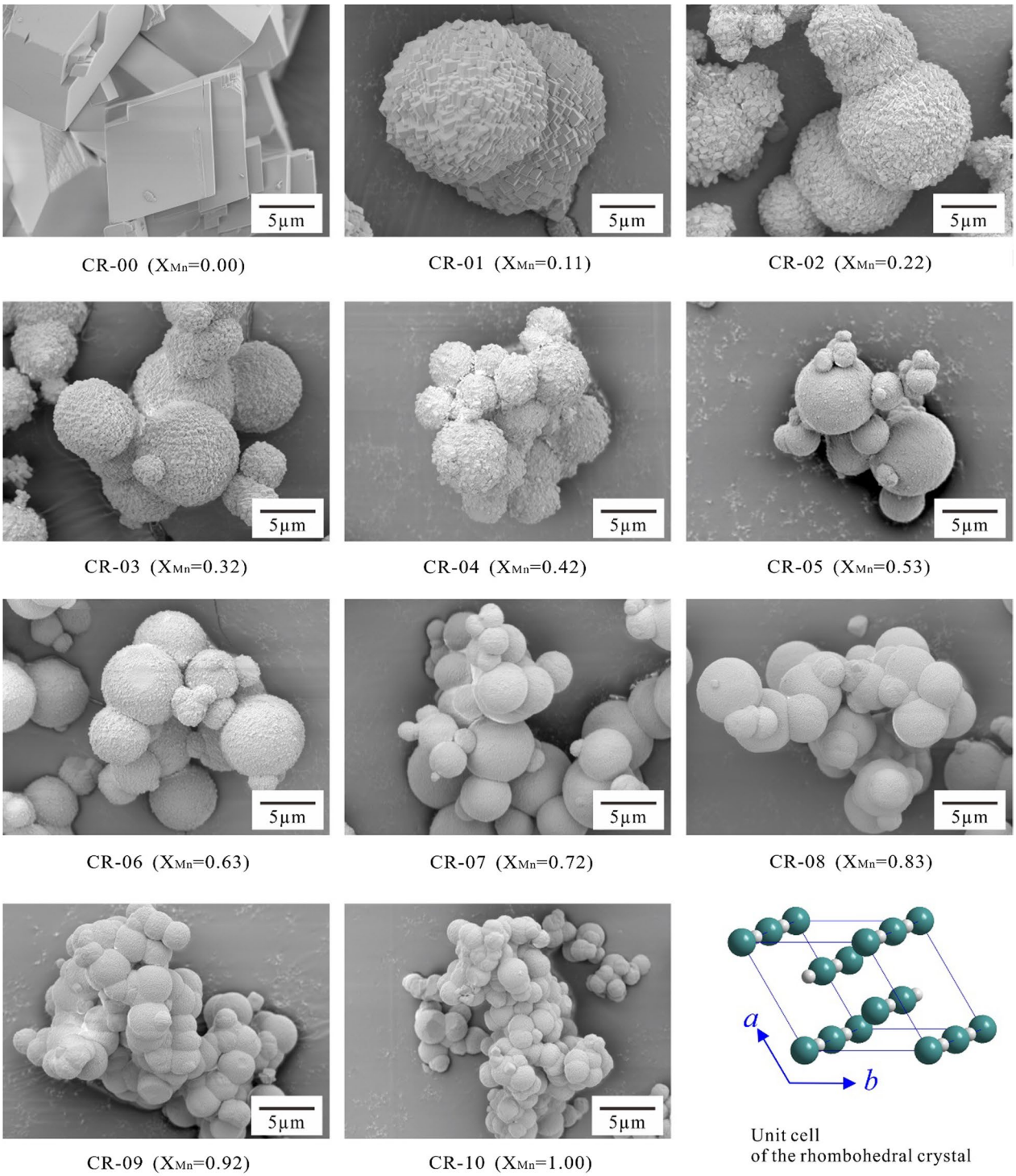

Fig. 2 SEM images of the $(Ca_{1-x}Mn_x)CO_3$ solid solutions before dissolution

molar ratio (X_{Mn}) during the dissolution of solids containing Mn (CR-01–CR-10). EDS analyses indicated that the acicular crystals or hexagonal prisms clearly had a higher Mn content than the bulk composition of the original solid (Additional file 1: Appendix S5). The rhodochrosite precipitate was monocrystalline [20, 29]. It was also observed that some rod-like phases formed

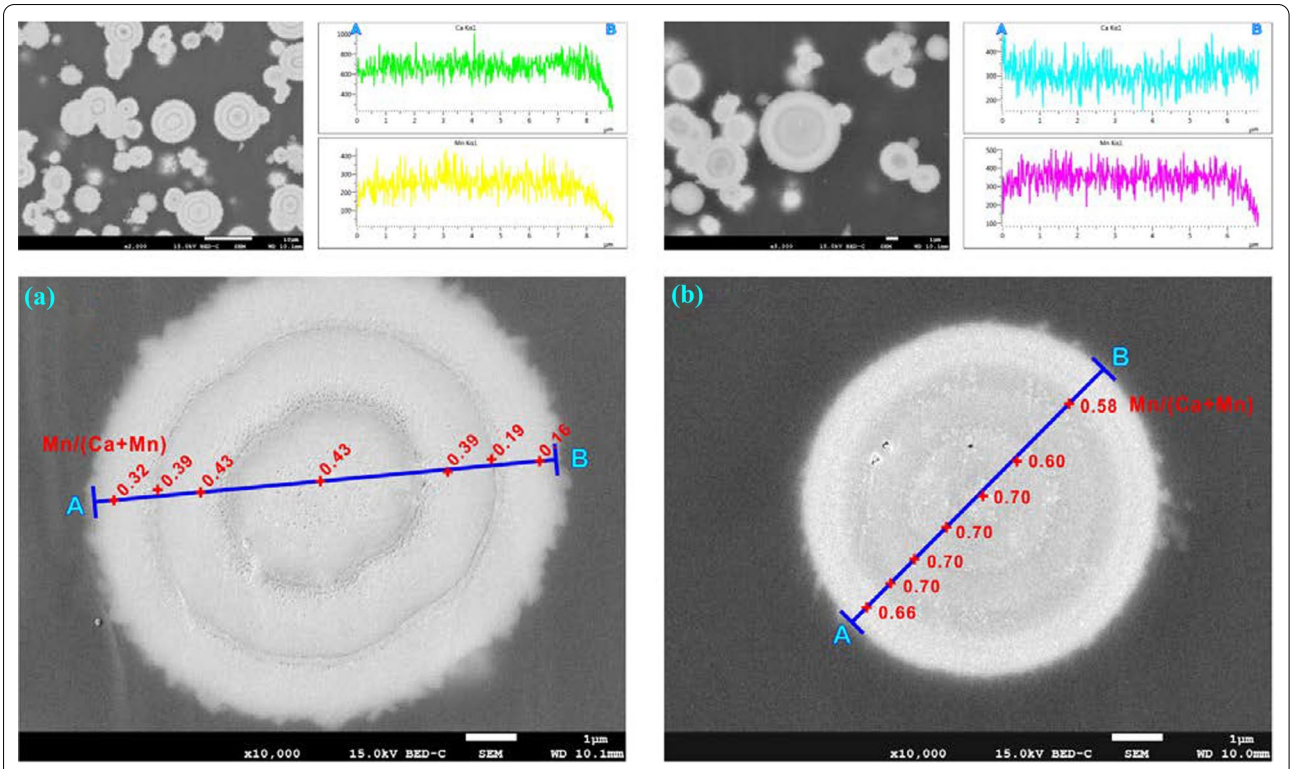

Fig. 3 BSE images of the equatorial sections and the corresponding compositional profiles along the A-B line of the (**a**) $(Ca_{0.68}Mn_{0.32})CO_3$ (CR-03) and (**b**) $(Ca_{0.48}Mn_{0.52})CO_3$ (CR-05) solids before dissolution

during the interaction between the calcite crystals and Mn^{2+} solution [30, 31].

Variation of the aqueous solution

Regarding dissolution in air-saturated water and N_2-degassed ultrapure water, the aqueous pH decreased gradually to a steady state (Figs. 6 and 7). The aqueous Ca and HCO_3+CO_3 concentrations increased up to the highest value after 1240–2400 h of dissolution for all $(Ca,Mn)CO_3$ solid solutions. The aqueous Mn concentrations increased up to the highest value of ~ 0.20 mmol/L after 1440 h and then decreased gradually to a steady state for pure rhodochrosite [$MnCO_3$] (CR-10). Regarding the Mn-containing solids (CR-01–CR-09), the aqueous Mn concentrations and the aqueous Mn/(Ca + Mn) mole ratios increased up to the highest value after 6–12 h of dissolution and then decreased gradually to a steady state (Additional file 1: Appendix S6). The X-ray photoelectron spectroscopy (XPS) analysis showed that Mn^{2+} ions were not oxidized during the dissolution in air-saturated initial solutions for the closed-system experiments (Additional file 1: Appendix S7).

Regarding dissolution in CO_2-saturated water, the aqueous pH increased rapidly from 4.26 of the starting solutions to 5.35–6.06 within 1 h of dissolution and then gradually reached a steady state (Fig. 8). Generally, the aqueous concentrations of Ca, Mn and HCO_3+CO_3 reached maximum values within 1 h of dissolution and then decreased to steady states with a slight fluctuation between 6 and 24 h. The aqueous Mn/(Ca + Mn) mole ratios increased up to the highest value after 1–6 h of dissolution and then decreased gradually to a steady state (Additional file 1: Appendix S6).

A large amount of the released Mn was eliminated from solutions, probably through reprecipitation/recrystallization. However, the Mn/(Ca + Mn) molar ratios in solution were clearly lower than X_{Mn} of the corresponding solid, indicating a nonstoichiometric release of Mn and Ca (Additional file 1: Appendix S6 and S8). It is also worth noting that the aqueous pH decreased and the aqueous Mn concentrations increased with an increasing X_{Mn} of the $(Ca,Mn)CO_3$ solid solutions. The aqueous Ca and HCO_3+CO_3 concentrations showed the highest values at $X_{Mn}=0.53$–0.63 (CR-05–CR-06) and then decreased as the X_{Mn} values decreased or increased (Additional file 1: Appendix S8).

The stoichiometric dissolution of the $(Ca_{1-x}Mn_x)CO_3$ solid solutions is as follows:

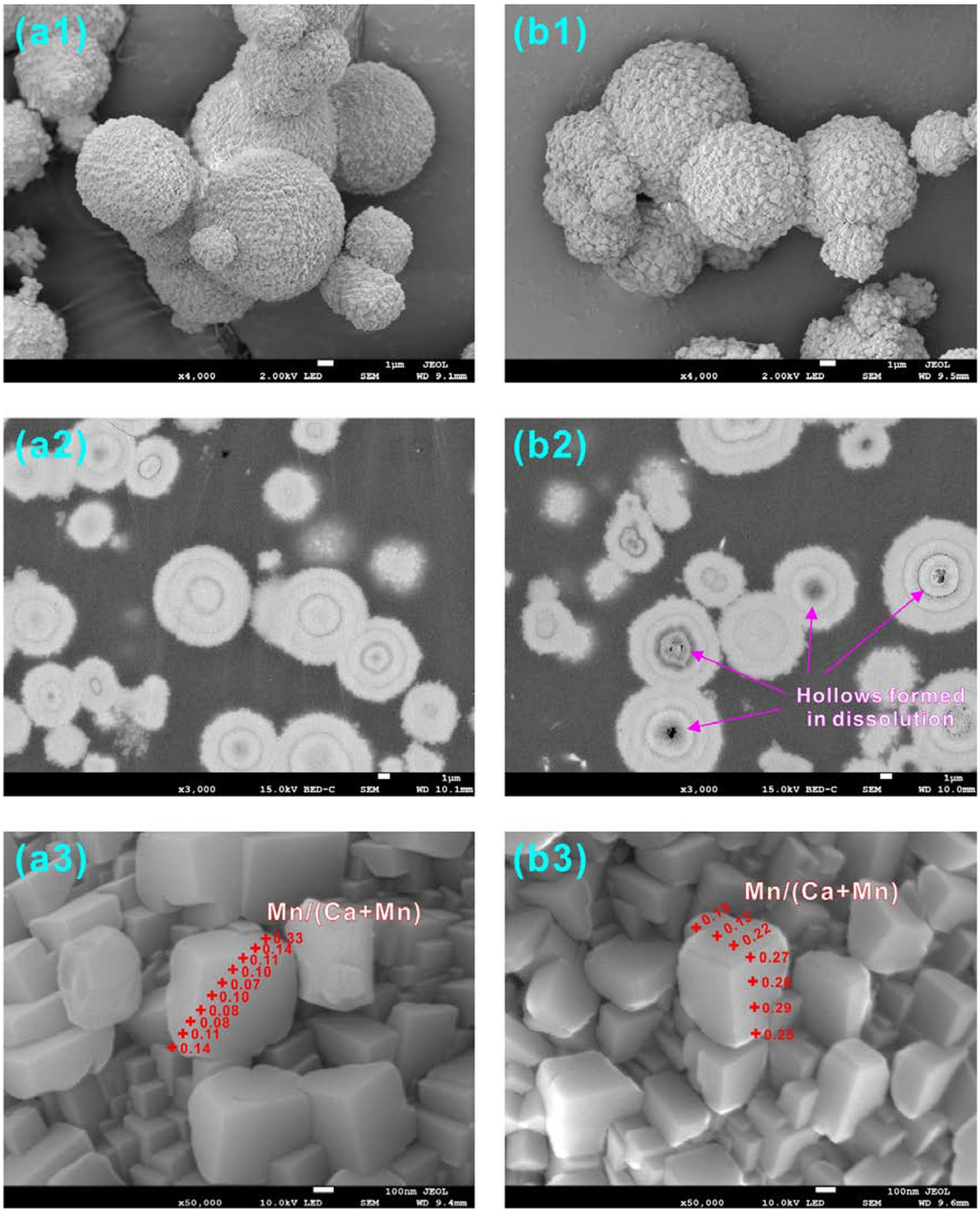

Fig. 4 SEM and BSE images of $(Ca_{0.68}Mn_{0.32})CO_3$ (CR-03) solid (**a**) before and (**b**) after dissolution in air-saturated water for 300 d

$$(Ca_{1-X}Mn_X)CO_3 = (1-X)Ca^{2+}_{(aq)} + XMn^{2+}_{(aq)} + CO^{2-}_{3(aq)} \quad (1)$$

$$Ca^{2+} + OH^- = Ca(OH)^+ \quad (2)$$

$$Mn^{2+} + nOH^- = Mn(OH)^{(n-2)-}_n \quad (n = 1 \sim 4) \quad (3)$$

$$Ca^{2+} + H^+ + CO^{2-}_3 = CaHCO^+_3 \quad (4)$$

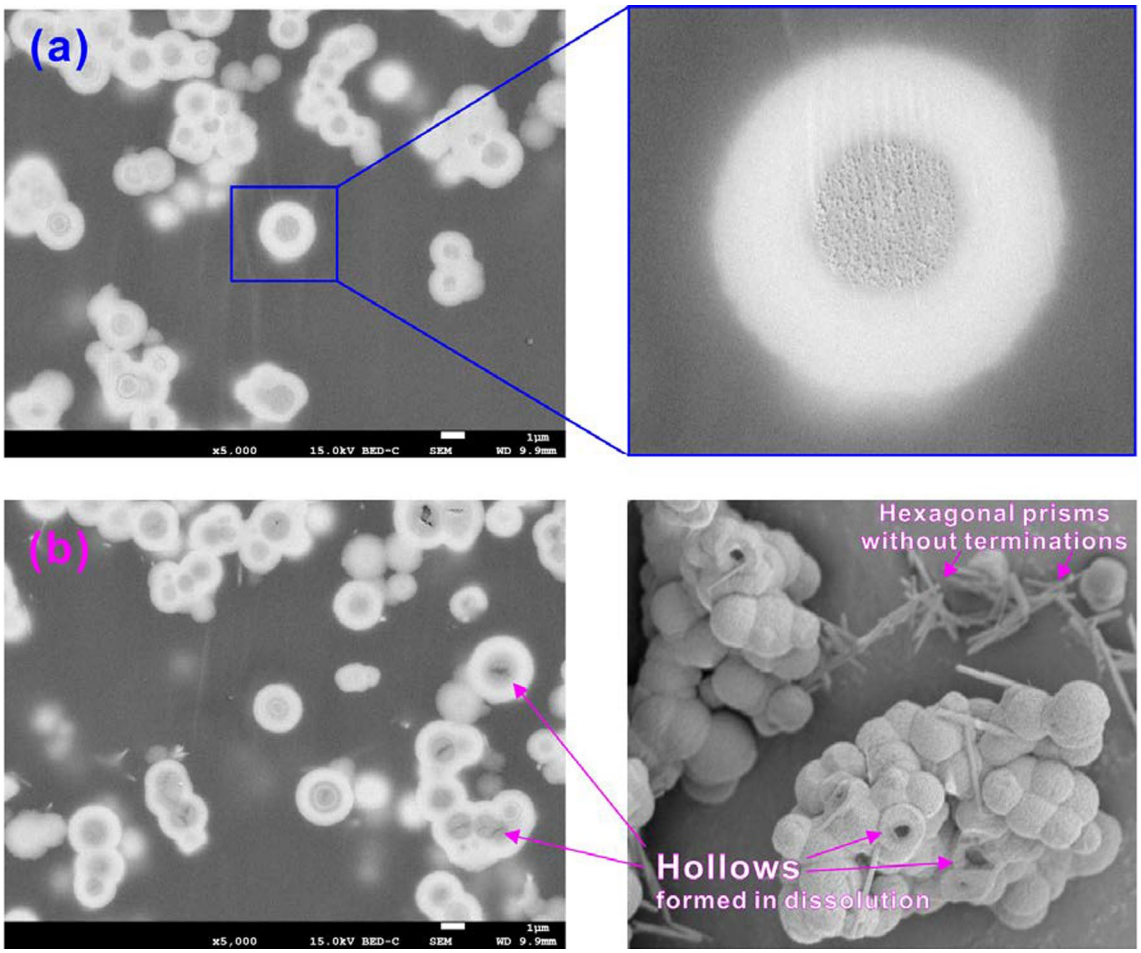

Fig. 5 SEM and BSE images of pure $MnCO_3$ (CR-10) (**a**) before and (**b**) after dissolution in air-saturated water for 300 d to show the formation of hollow spheres and hexagonal prisms without terminations

$$Mn^{2+} + H^+ + CO_3^{2-} = MnHCO_3^+ \quad (5)$$

$$CO_3^{2-} + nH^+ = H_nCO_3^{(2-n)-} \quad (n = 1, 2) \quad (6)$$

At the early stage, all components were dissolved stoichiometrically (Eq. (1)). Regarding the dissolution in N_2-degassed water and air-saturated water, the pH decrease was ascribed to the formation of $Ca(OH)^+$ and $Mn(OH)_n^{(n-2)-}$ (Eqs. (2) and (3)), which resulted in OH^- depletion. Regarding the dissolution in CO_2-saturated water, the pH increase was ascribed to the formation of $CaHCO_3^+$, $MnHCO_3^+$ and $H_nCO_3^{(2-n)-}$ (Eqs. (4)–(6)), which resulted in H^+ depletion. The notable pH variation showed that the initial dissolution was pH-controlled [20, 32]. More calcium was dissolved than manganese, indicating that the $(Ca_{1-x}Mn_x)CO_3$ solid solutions dissolved nonstoichiometrically [20] and suggesting the existence of an interfacial dissolution–precipitation process; thus, manganese more favorably nucleated on the crystal surfaces to form new precipitates [20, 33].

Determination of the stoichiometric solubility

Dissolution was carried out until the differences in the calculated IAP values for the final three solutions (i.e., 2400 h, 4800 h and 7200 h; assuming a steady state was reached) were mostly within ± 0.25 log units [34]. The PHREEQC simulation results indicated that all aqueous solutions in the present research were undersaturated with respect to any probable secondary mineral phases, including portlandite [$Ca(OH)_2$, saturation indexes (SI) = − 6.68 ~ − 15.10] and pyrochroite [$Mn(OH)_2$, SI = − 1.27 ~ − 14.98].

The thermodynamic solubility product could be calculated from the long-term steady states or extrapolated ion activity products (IAPs) of the solutions that corresponded to the equilibrium constant of mineral

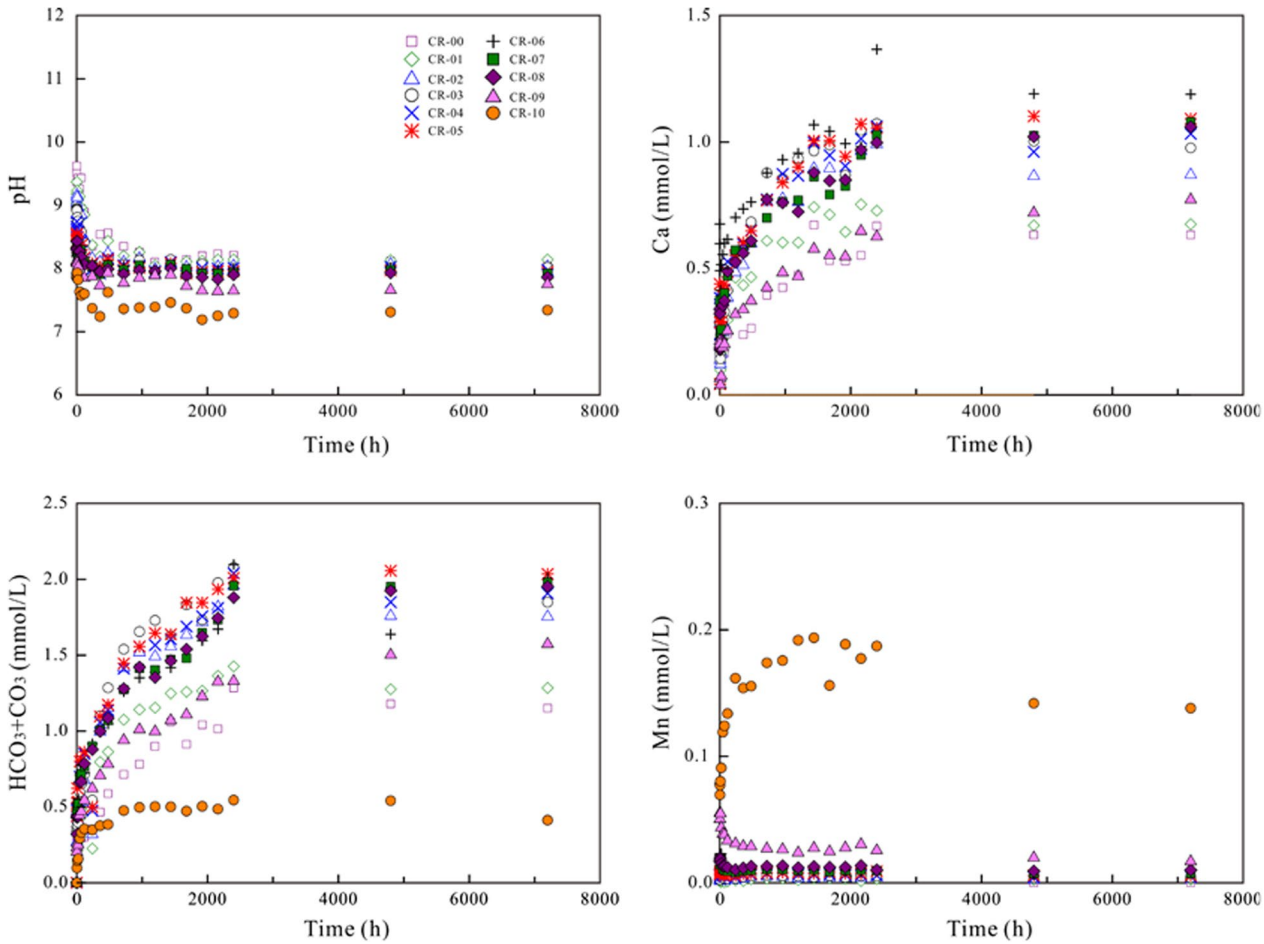

Fig. 6 Variation in the aqueous pH and components during the dissolution of the $(Ca_{1-x}Mn_x)CO_3$ solid solutions in air-saturated water

dissolution [6]. The equilibrium constant (K_{sp}, the stoichiometric solubility product) of the dissolution after Eq. (1) at dissolution equilibrium can be estimated by Eq. (7):

$$K_{sp} = \mathrm{IAP} = \left\{Ca^{2+}\right\}^{1-x}\left\{Mn^{2+}\right\}^{x}\left\{CO_3^{2-}\right\} \quad (7)$$

where {} is the free ion activity.

The standard free energy of reaction (ΔG_r^o) can be calculated from K_{sp} at 298.15 K and 0.101 MPa with Eq. (8):

$$\Delta G_r^\circ = -5.708 \log\_K_{sp} \quad (8)$$

For Eq. (1),

$$\Delta G_r^\circ = (1-x)\Delta G_f^\circ\left[Ca^{2+}\right] + x\Delta G_f^\circ\left[Mn^{2+}\right] + \Delta G_f^\circ\left[CO_3^{2-}\right] - \Delta G_f^\circ[(Ca_{1-x}Mn_x)CO_3] \quad (9)$$

Rearranging, we obtain:

$$\Delta G_f^\circ[(Ca_{1-x}Mn_x)CO_3] = (1-x)\Delta G_f^\circ\left[Ca^{2+}\right] + x\Delta G_f^\circ\left[Mn^{2+}\right] + \Delta G_f^\circ\left[CO_3^{2-}\right] - \Delta G_r^\circ \quad (10)$$

Tables 2, 3 and 4 list the pH, Ca, Mn and HCO_3^-/CO_3^{2-} analytical results and the calculated log_IAP values at the final steady state ($\approx \log\_K_{sp}$) for the $(Ca_{1-x}Mn_x)CO_3$ solid solutions. Based on the obtained literature data, $\Delta G_f^\circ[Ca^{2+}] = -553.54$ kJ/mol, $\Delta G_f^\circ[Mn^{2+}] = -228$ kJ/mol and $\Delta G_f^\circ[CO_3^{2-}] = -527.9$ kJ/mol [35], the free energies of formation, $\Delta G_f^\circ[(Ca_{1-x}Mn_x)CO_3]$, were also estimated.

Regarding the dissolution in N_2-degassed, air-saturated and CO_2-saturated ultrapure waters at

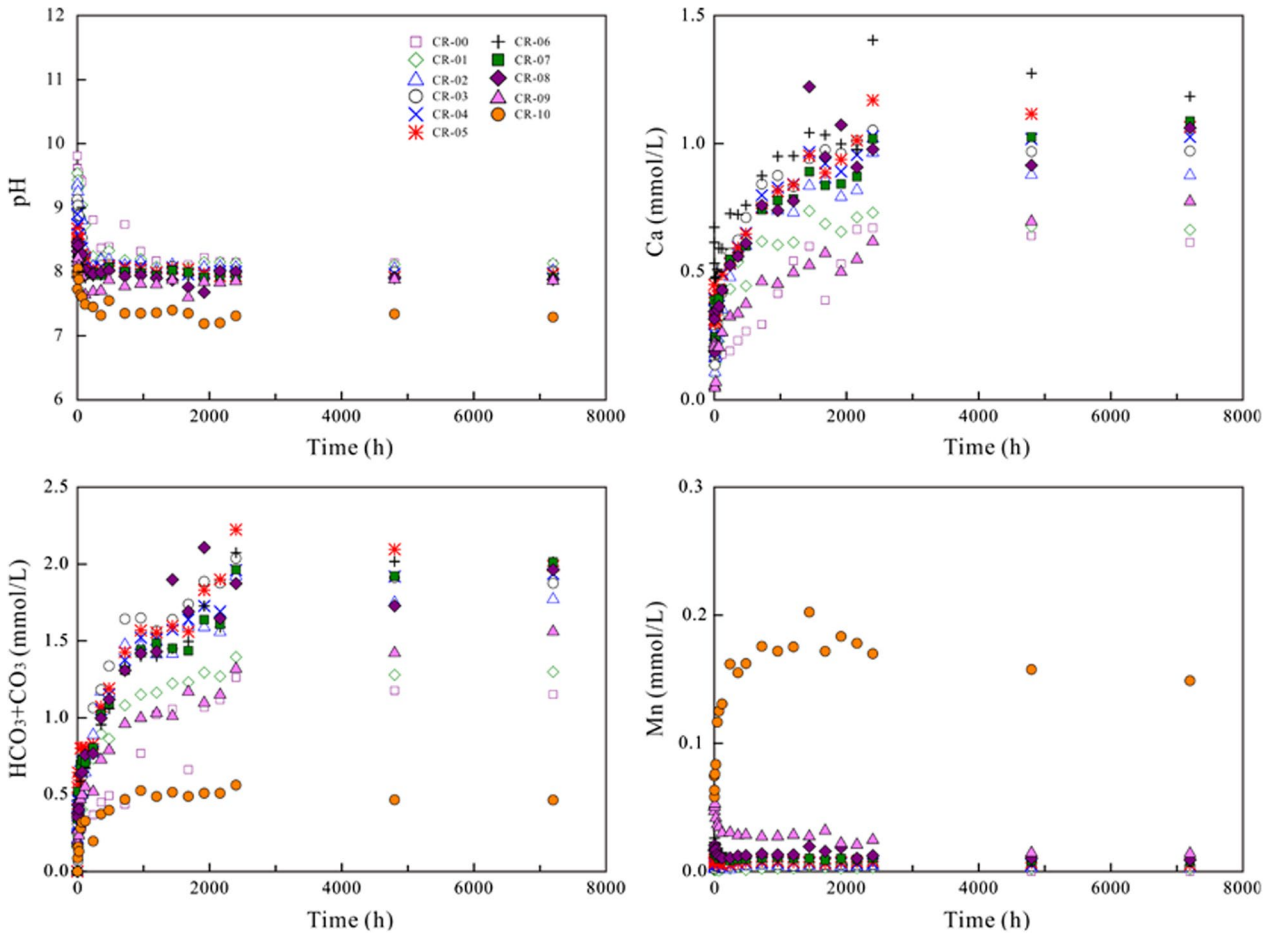

Fig. 7 Variation in the aqueous pH and components during the dissolution of the $(Ca_{1-x}Mn_x)CO_3$ solid solutions in N_2-degassed water

25 °C, the average log_IAP values at the final steady state (≈log_K_{sp}) were estimated to be −8.46 ± 0.06, −8.44 ± 0.10 and -8.59 ± 0.10, respectively, for calcite [$CaCO_3$] with ΔG_f° values of −1129.71 ± 0.30 kJ/mol, −1129.63 ± 0.59 kJ/mol and −1130.48 ± 0.57 kJ/mol, respectively. These results were consistent with the various K_{sp} and ΔG_f° values for $CaCO_3$ found in the literature. For instance, both the minteq.v4.dat database and the phreeqc.dat database showed a log_K_{sp} of −8.48 [21, 36, 37]. Additionally, $CaCO_3$ has a very well-defined solubility product (log_K_{sp}) reported to fall within −8.30 [14, 38].

Regarding the dissolution in N_2-degassed, air-saturated and CO_2-saturated ultrapure waters at 25 °C, the average log_IAP values at the final steady state (≈log_K_{sp}) were estimated to be −10.25 ± 0.08, −10.26 ± 0.10 and −10.28 ± 0.03, respectively, for rhodochrosite [$MnCO_3$] with ΔG_f° values of −814.39 ± 0.44 kJ/mol, −814.46 ± 0.54 kJ/mol and −814.59 ± 0.20 kJ/mol, respectively. Many inconsistent values of the solubility product for rhodochrosite [$MnCO_3$] have been reported in the literature [11]. Some of the log_K_{sp} values for $MnCO_3$ reported are −9.47 [5], −10.06 [39], −10.30 [3], −10.41 [13], −10.42 [40], −10.55 [41], −10.62 [42], −10.76 [43], −10.99 [14], −11.39 ~ −11.65 [38] and −12.19 [44]. The various ΔG_f° values for $MnCO_3$(s) found in the literature ranged from −809.89 ± 0.73 kJ/mol [5] to −818.81 kJ/mol [14], including −812.53 kJ/mol [45], −813.0 kJ/mol [39], −814.6 kJ/mol [14], −816.05 ± 1.38 kJ/mol [46], −816.32 ± 0.07 kJ/mol [41], −816.6 ± 0.2 kJ/mol [47] and −816.7 kJ/mol [42]. As a result, a large difference among the log_K_{sp} values for rhodochrosite could also be found in various databases. For instance, whereas the minteq.v4.dat database [36] showed a log_K_{sp} of −10.58, the phreeqc.dat database had a log_K_{sp} of −11.13 [21, 37]. A log_K_{sp} of −10.50 is usually accepted in the geochemical literature [48]. The disparity in the published thermodynamic solubility products arose from the lack of

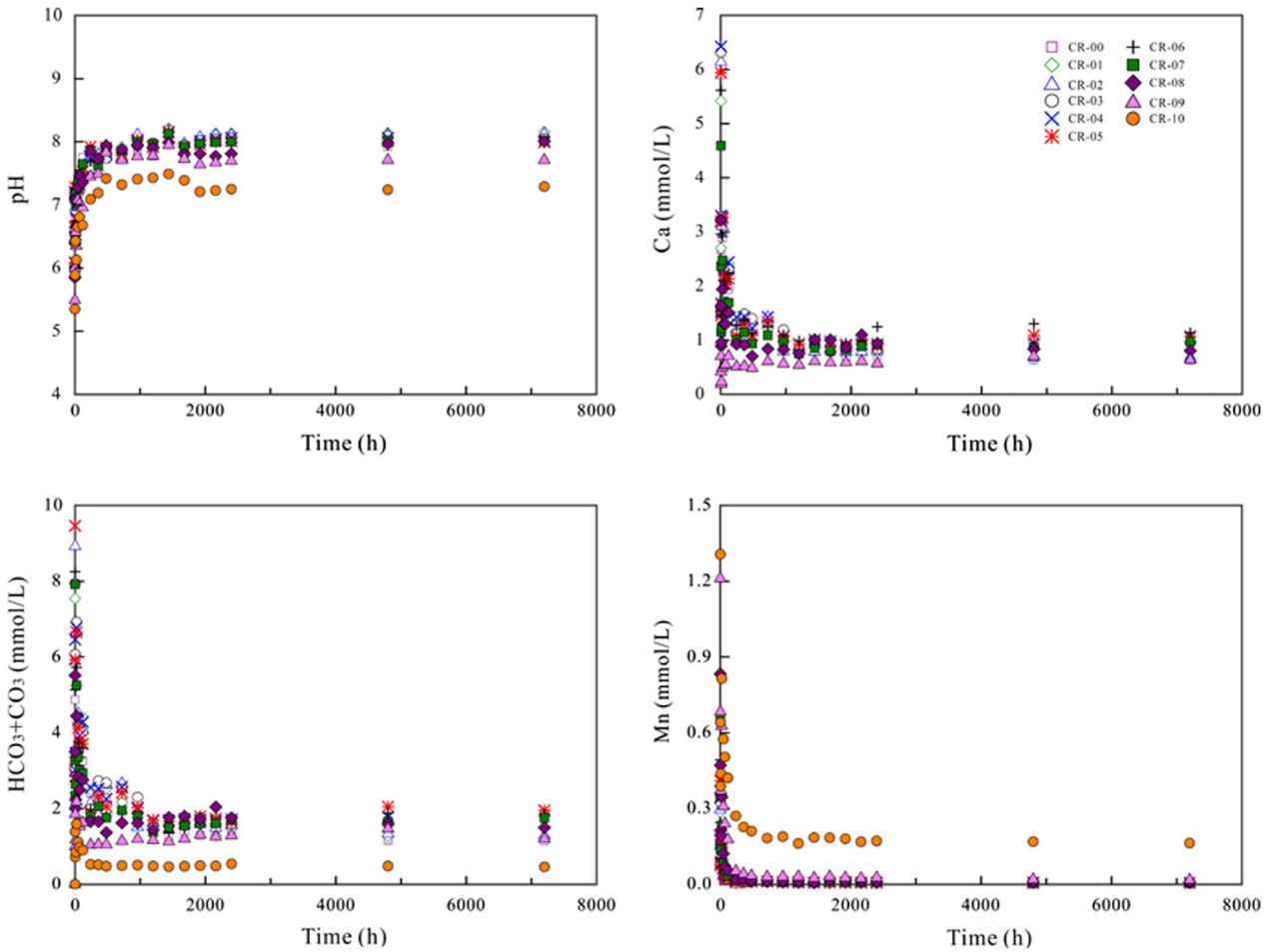

Fig. 8 Variation in the aqueous pH and components during the dissolution of the $(Ca_{1-x}Mn_x)CO_3$ solid solutions in CO_2-saturated water

experimental analyses and their derivation/extrapolation, from the differences in the involved aqueous speciations [49] or from the impurities in solid samples [5].

As the X_{Mn} of the $(Ca_{1-x}Mn_x)CO_3$ solid solutions increased, the log_IAP values at the final steady state decreased from $-8.44 \sim -8.59$ for calcite to $-10.25 \sim -10.28$ for rhodochrosite (Tables 2, 3 and 4). These values were consistent with $\log\_K_{sp} = -9.3$ for $Mn_{25}Ca_{0.75}CO_3$ and log_IAP of -9.9 for $Mn_{0.48}Ca_{0.52}CO_3$ obtained from dissolution experiments [4]. The disordered calcian rhodochrosite ($Mn_{0.58}Ca_{0.39}Mg_{0.03}CO_3$) precipitated in the laboratory showed a log_IAP value of -10.38 after long-term equilibration [6]. The solubilities of the $Mn_xCa_{1-x}CO_3$ solid solutions in the present work were generally lower than the data calculated using the empirical expression derived from the experimental electrochemical cell data [5], which was related to the ΔG_f° value of -809.89 ± 0.73 kJ/mol for $MnCO_3$ being too large in comparison to those ($-812.53 \sim -818.81$ kJ/mol) in the present work and other studies [14, 39, 41, 42, 45–47].

Lippmann diagram

Construction of the Lippmann diagram

The solid solution–aqueous solution (SS-AS) system is of essential importance to understand the geochemical process. Despite many studies, thermodynamic data about the SS-AS interaction are still scarce. The methods to construct Lippmann diagrams have been described in detail in numerous works covering a wide variety of SS-AS systems [2, 10, 25, 26, 28, 34, 50–56].

The Lippmann diagram is a graph that shows the "*solidus*" and "*solutus*" phase relationship in an SS-AS system. The "total activity product" ($\Sigma\Pi_{SS}$) is defined as the sum of the partial activity products of the end-members at equilibrium. The "*solidus*" and "*solutus*" curves are the plots of $\Sigma\Pi_{SS}$ versus the solid component and the solution component, which define all probable

Table 2 Analytical data and solubility of the $(Ca_{1-x}Mn_x)CO_3$ solid solutions in air-saturated water at 25 °C

Sample	Dissolution time (h)	pH	Concentration (mmol/L)			log_IAP[c]	Average log_IAP	ΔG_f° (kJ/mol)	Average ΔG_f° (kJ/mol)
			Ca	Mn	$HCO_3 + CO_3$				
$(Ca_{1.00}Mn_{0.00})CO_3$	2400	8.21	0.6677	0.0000	1.2831	−8.34	−8.44	−1129.04	−1129.63
	4800	8.12	0.6330	0.0000	1.1790	−8.48	±0.10	−1129.87	±0.59
	7200	8.11	0.6323	0.0000	1.1507	−8.50		−1129.98	
$(Ca_{0.89}Mn_{0.11})CO_3$[a]	2400	8.14	0.7281	0.0031	1.4260	−8.62	−8.68	−1094.68	−1095.02
$(Ca_{0.88}Mn_{0.12})CO_3$[b]	4800	8.13	0.6702	0.0023	1.2751	−8.72	±0.06	−1095.24	±0.34
	7200	8.14	0.6749	0.0025	1.2841	−8.70		−1095.13	
$(Ca_{0.78}Mn_{0.22})CO_3$[a]	2400	8.04	0.9911	0.0046	1.9561	−8.74	−8.83	−1059.46	−1059.92
$(Ca_{0.76}Mn_{0.24})CO_3$[b]	4800	8.07	0.8657	0.0026	1.7596	−8.85	±0.08	−1060.06	±0.46
	7200	8.03	0.8708	0.0030	1.7536	−8.88		−1060.22	
$(Ca_{0.68}Mn_{0.32})CO_3$[a]	2400	7.99	1.0729	0.0052	2.0771	−8.99	−9.04	−1028.19	−1028.46
$(Ca_{0.65}Mn_{0.35})CO_3$[b]	4800	8.01	1.0029	0.0039	1.9388	−9.06	±0.05	−1028.55	±0.27
	7200	8.02	0.9766	0.0039	1.8492	−9.07		−1028.64	
$(Ca_{0.58}Mn_{0.42})CO_3$[a]	2400	8.01	1.0624	0.0057	2.0395	−9.21	−9.28	−996.79	−997.16
$(Ca_{0.54}Mn_{0.46})CO_3$[b]	4800	8.02	0.9609	0.0043	1.8495	−9.32	±0.07	−997.37	±0.37
	7200	7.98	1.0321	0.0049	1.9072	−9.31		−997.31	
$(Ca_{0.47}Mn_{0.53})CO_3$[a]	2400	7.96	1.0554	0.0091	2.0089	−9.39	−9.45	−962.13	−962.49
$(Ca_{0.44}Mn_{0.56})CO_3$[b]	4800	7.97	1.1016	0.0058	2.0568	−9.47	±0.07	−962.57	±0.36
	7200	7.94	1.0914	0.0058	2.0347	−9.51		−962.78	
$(Ca_{0.37}Mn_{0.63})CO_3$[a]	2400	8.00	1.4088	0.0100	2.0973	−9.48	−9.62	−930.11	−930.87
$(Ca_{0.34}Mn_{0.66})CO_3$[b]	4800	8.01	1.1903	0.0062	1.6380	−9.73	±0.13	−931.48	±0.76
	7200	7.96	1.1889	0.0073	2.0109	−9.64		−931.02	
$(Ca_{0.28}Mn_{0.72})CO_3$[a]	2400	7.93	1.0275	0.0095	1.9579	−9.79	−9.82	−902.68	−902.89
$(Ca_{0.26}Mn_{0.74})CO_3$[b]	4800	7.98	1.0251	0.0074	1.9515	−9.82	±0.05	−902.84	±0.26
	7200	7.92	1.0789	0.0074	1.9774	−9.87		−903.14	
$(Ca_{0.17}Mn_{0.83})CO_3$[a]	2400	7.90	0.9976	0.0102	1.8802	−10.01	−10.02	−868.28	−868.33
$(Ca_{0.16}Mn_{0.84})CO_3$[b]	4800	7.93	1.0205	0.0092	1.9245	−10.01	±0.02	−868.26	±0.11
	7200	7.86	1.0598	0.0101	1.9521	−10.04		−868.44	
$(Ca_{0.08}Mn_{0.92})CO_3$[a]	2400	7.65	0.6258	0.0256	1.3296	−10.21	−10.23	−840.16	−840.23
$(Ca_{0.07}Mn_{0.93})CO_3$[b]	4800	7.66	0.7201	0.0199	1.5022	−10.26	±0.03	−840.40	±0.17
	7200	7.75	0.7722	0.0169	1.5735	−10.21		−840.13	
$(Ca_{0.00}Mn_{1.00})CO_3$	2400	7.29	0.0000	0.1871	0.5449	−10.16	−10.26	−813.92	−814.46
	4800	7.31	0.0000	0.1419	0.5413	−10.26	±0.10	−814.47	±0.54
	7200	7.34	0.0000	0.1380	0.4123	−10.35		−815.00	

[a] Bulk composition before dissolution; [b]Bulk composition after 300 d of dissolution;

[c] IAP estimated for the bulk composition after 300 d of dissolution

thermodynamic saturation states as a function of the solid and aqueous components, respectively.

Regarding the calcite-rhodochrosite solid solutions $[(Ca_{1-x}Mn_x)CO_3]$, the "*solidus*" curve is described by

$$\sum\prod_{SS} = \left(\left\{Ca^{2+}\right\} + \left\{Mn^{2+}\right\}\right)\left\{CO_3^{2-}\right\} = K_{Ca}X_{Ca}\gamma_{Ca} + K_{Mn}X_{Mn}\gamma_{Mn} \quad (11)$$

where {} designates aqueous activity. K_{Ca} and K_{Mn}, X_{Ca} and X_{Mn}, γ_{Ca} and γ_{Mn} are the solubility products, the molar ratios (x, 1−x) and the activity coefficients of $CaCO_3$ and $MnCO_3$ in the $(Ca_{1-x}Mn_x)CO_3$ solid solutions, respectively.

The "*solutus*" curve is expressed by:

$$\sum\prod_{SS} = \frac{1}{\frac{X_{Ca^{2+},aq}}{K_{Ca}\gamma_{Ca}} + \frac{X_{Mn^{2+},aq}}{K_{Mn}\gamma_{Mn}}} \quad (12)$$

where $X_{Ca^{2+},aq}$ and $X_{Mn^{2+},aq}$ are the activity ratios of aqueous Ca^{2+} and Mn^{2+}, respectively.

Table 3 Analytical data and solubility of the $(Ca_{1-x}Mn_x)CO_3$ solid solutions in N_2-degassed water at 25 °C

Sample	Dissolution time (h)	pH	Concentration (mmol/L)			log_IAP[c]	Average log_IAP	$\Delta G_f°$ (kJ/mol)	Average $\Delta G_f°$ (kJ/mol)
			Ca	Mn	$HCO_3 + CO_3$				
$(Ca_{1.00}Mn_{0.00})CO_3$	2400	8.15	0.6712	0.0000	1.2626	−8.40	−8.46	−1129.41	−1129.71
	4800	8.14	0.6405	0.0000	1.1771	−8.46	±0.06	−1129.73	±0.30
	7200	8.12	0.6146	0.0000	1.1512	−8.51		−1129.99	
$(Ca_{0.89}Mn_{0.11})CO_3$[a]	2400	8.14	0.7306	0.0029	1.3955	−8.63	−8.70	−1094.74	−1095.12
$(Ca_{0.88}Mn_{0.12})CO_3$[b]	4800	8.11	0.6762	0.0021	1.2796	−8.74	±0.07	−1095.36	±0.38
	7200	8.13	0.6635	0.0019	1.2983	−8.72		−1095.27	
$(Ca_{0.78}Mn_{0.22})CO_3$[a]	2400	8.07	0.9646	0.0041	1.9198	−8.74	−8.83	−1059.45	−1059.96
$(Ca_{0.76}Mn_{0.24})CO_3$[b]	4800	8.05	0.8793	0.0028	1.7496	−8.86	±0.09	−1060.14	±0.51
	7200	8.02	0.8767	0.0027	1.7703	−8.89		−1060.30	
$(Ca_{0.68}Mn_{0.32})CO_3$[a]	2400	7.99	1.0529	0.0053	2.0362	−8.98	−9.03	−1028.24	−1028.56
$(Ca_{0.66}Mn_{0.34})CO_3$[b]	4800	8.00	0.9690	0.0041	1.9116	−9.05	±0.06	−1028.66	±0.32
	7200	8.00	0.9715	0.0037	1.8750	−9.07		−1028.78	
$(Ca_{0.58}Mn_{0.42})CO_3$[a]	2400	8.00	1.0290	0.0060	1.9608	−9.21	−9.26	−996.92	−997.17
$(Ca_{0.55}Mn_{0.45})CO_3$[b]	4800	7.97	1.0181	0.0053	1.9182	−9.28	±0.05	−997.29	±0.25
	7200	7.98	1.0265	0.0048	1.9362	−9.28		−997.30	
$(Ca_{0.47}Mn_{0.53})CO_3$[a]	2400	7.93	1.1697	0.0080	2.2236	−9.37	−9.44	−962.15	−962.54
$(Ca_{0.45}Mn_{0.55})CO_3$[b]	4800	7.92	1.1162	0.0066	2.0954	−9.46	±0.07	−962.62	±0.38
	7200	7.96	1.0650	0.0054	1.9879	−9.49		−962.83	
$(Ca_{0.37}Mn_{0.63})CO_3$[a]	2400	7.96	1.4048	0.0107	2.0743	−9.49	−9.61	−930.26	−930.93
$(Ca_{0.35}Mn_{0.65})CO_3$[b]	4800	7.89	1.2750	0.0078	2.0165	−9.67	±0.12	−931.27	±0.67
	7200	7.92	1.1846	0.0073	2.0147	−9.66		−931.26	
$(Ca_{0.28}Mn_{0.72})CO_3$[a]	2400	7.92	1.0190	0.0104	1.9639	−9.75	−9.82	−902.58	−902.97
$(Ca_{0.27}Mn_{0.73})CO_3$[b]	4800	7.90	1.0256	0.0081	1.9219	−9.85	±0.07	−903.18	±0.39
	7200	7.90	1.0883	0.0077	2.0129	−9.85		−903.15	
$(Ca_{0.17}Mn_{0.83})CO_3$[a]	2400	8.00	0.9781	0.0124	1.8736	−9.84	−9.98	−867.32	−868.09
$(Ca_{0.16}Mn_{0.84})CO_3$[b]	4800	7.91	0.9155	0.0102	1.7284	−10.04	±0.13	−868.42	±0.76
	7200	7.88	1.0614	0.0092	1.9629	−10.05		−868.51	
$(Ca_{0.08}Mn_{0.92})CO_3$[a]	2400	7.85	0.6178	0.0246	1.3181	−10.01	−10.11	−839.09	−839.66
$(Ca_{0.08}Mn_{0.92})CO_3$[b]	4800	7.88	0.6963	0.0145	1.4213	−10.16	±0.10	−839.95	±0.56
	7200	7.86	0.7745	0.0140	1.5604	−10.16		−839.93	
$(Ca_{0.00}Mn_{1.00})CO_3$	2400	7.31	0.0000	0.1700	0.5620	−10.17	−10.25	−813.95	−814.39
	4800	7.34	0.0000	0.1576	0.4657	−10.25	±0.08	−814.39	±0.44
	7200	7.29	0.0000	0.1489	0.4647	−10.33		−814.84	

[a] Bulk composition before dissolution; [b]Bulk composition after 300 d of dissolution

[c] IAP estimated for the bulk composition after 300 d of dissolution

Regarding the members of fixed $X_{Ca} = 1\text{-}X_{Mn}$, a set of minimum stoichiometric saturation curves in terms of $X_{Ca^{2+},aq}$ are expressed by:

$$\sum \prod_{SS} = \frac{IAP}{(X_{Ca^{2+},aq})^{X_{Ca}} (X_{Mn^{2+},aq})^{X_{Mn}}} \quad (13)$$

Regarding the endmembers $CaCO_3$ and $MnCO_3$, $X_{Ca} = 1$ and $X_{Ca} = 0$, the endmember saturation curves are described by:

$$\sum \prod_{CaCO_3} = \frac{\{Ca^{2+}\}\{CO_3^{2-}\}}{(X_{Ca^{2+},aq})^{X_{Ca}}} = \frac{K_{Ca}}{(X_{Ca^{2+},aq})^{X_{Ca}}} \quad (14)$$

$$\sum \prod_{MnCO_3} = \frac{\{Mn^{2+}\}\{CO_3^{2-}\}}{\left(X_{Mn^{2+},aq}\right)^{X_{Mn}}} = \frac{K_{Mn}}{\left(X_{Mn^{2+},aq}\right)^{X_{Mn}}} \quad (15)$$

Table 4 Analytical data and solubility of the $(Ca_{1-x}Mn_x)CO_3$ solid solutions in CO_2-saturated water at 25 °C

Sample	Dissolution time (h)	pH	Concentration (mmol/L)			log_IAP[c]	Average log_IAP	ΔG_f° (kJ/mol)	Average ΔG_f° (kJ/mol)
			Ca	Mn	$HCO_3 + CO_3$				
$(Ca_{1.00}Mn_{0.00})CO_3$	2400	8.00	0.7096	0.0000	1.3379	−8.51	−8.59	−1130.00	−1130.48
	4800	7.92	0.6304	0.0000	1.1650	−8.69	±0.10	−1131.05	±0.57
	7200	8.04	0.6315	0.0000	1.1547	−8.57		−1130.38	
$(Ca_{0.89}Mn_{0.11})CO_3$[a]	2400	8.13	0.7705	0.0030	1.4653	−8.60	−8.66	−1094.57	−1094.93
$(Ca_{0.88}Mn_{0.12})CO_3$[b]	4800	8.14	0.6686	0.0032	1.2606	−8.69	±0.06	−1095.12	±0.36
	7200	8.16	0.6512	0.0033	1.2451	−8.69		−1095.09	
$(Ca_{0.78}Mn_{0.22})CO_3$[a]	2400	8.11	0.7954	0.0039	1.5584	−8.85	−8.92	−1060.05	−1060.50
$(Ca_{0.76}Mn_{0.24})CO_3$[b]	4800	8.11	0.6830	0.0039	1.3393	−8.95	±0.08	−1060.66	±0.45
	7200	8.12	0.6593	0.0038	1.2771	−8.97		−1060.79	
$(Ca_{0.68}Mn_{0.32})CO_3$[a]	2400	8.06	0.8304	0.0054	1.5895	−9.08	−9.05	−1028.73	−1028.53
$(Ca_{0.65}Mn_{0.35})CO_3$[b]	4800	8.09	0.8764	0.0046	1.6778	−9.04	±0.03	−1028.49	±0.20
	7200	8.05	0.9419	0.0048	1.8336	−9.02		−1028.38	
$(Ca_{0.58}Mn_{0.42})CO_3$[a]	2400	8.06	0.9222	0.0057	1.7134	−9.24	−9.23	−997.07	−997.03
$(Ca_{0.55}Mn_{0.45})CO_3$[b]	4800	8.06	0.9464	0.0054	1.7810	−9.23	±0.01	−997.00	±0.04
	7200	8.01	1.0500	0.0052	1.9438	−9.23		−997.02	
$(Ca_{0.47}Mn_{0.53})CO_3$[a]	2400	8.01	0.8893	0.0058	1.6451	−9.55	−9.47	−963.04	−962.60
$(Ca_{0.44}Mn_{0.56})CO_3$[b]	4800	8.01	1.0871	0.0069	2.0502	−9.39	±0.08	−962.13	±0.46
	7200	7.99	1.0713	0.0058	1.9531	−9.48		−962.61	
$(Ca_{0.37}Mn_{0.63})CO_3$[a]	2400	7.98	1.2446	0.0101	1.6866	−9.58	−9.61	−930.78	−930.96
$(Ca_{0.35}Mn_{0.65})CO_3$[b]	4800	7.95	1.3037	0.0085	1.8842	−9.61	±0.03	−930.94	±0.19
	7200	7.99	1.1368	0.0070	1.8409	−9.64		−931.14	
$(Ca_{0.28}Mn_{0.72})CO_3$[a]	2400	8.00	0.9182	0.0105	1.7070	−9.77	−9.82	−902.46	−902.74
$(Ca_{0.25}Mn_{0.75})CO_3$[b]	4800	8.02	0.8777	0.0084	1.6451	−9.84	±0.05	−902.85	±0.28
	7200	8.02	0.9792	0.0073	1.7481	−9.85		−902.92	
$(Ca_{0.17}Mn_{0.83})CO_3$[a]	2400	7.81	0.9402	0.0105	1.7566	−10.12	−10.05	−868.91	−868.51
$(Ca_{0.16}Mn_{0.84})CO_3$[b]	4800	7.97	0.8331	0.0108	1.5837	−10.00	±0.07	−868.19	±0.40
	7200	8.01	0.8028	0.0091	1.4962	−10.04		−868.44	
$(Ca_{0.08}Mn_{0.92})CO_3$[a]	2400	7.70	0.5699	0.0264	1.2909	−10.16	−10.24	−839.86	−840.32
$(Ca_{0.07}Mn_{0.93})CO_3$[b]	4800	7.71	0.6976	0.0196	1.4666	−10.22	±0.11	−840.18	±0.60
	7200	7.71	0.6368	0.0174	1.1982	−10.35		−840.93	
$(Ca_{0.00}Mn_{1.00})CO_3$	2400	7.25	0.0000	0.1717	0.5410	−10.25	−10.28	−814.39	−814.59
	4800	7.24	0.0000	0.1687	0.4840	−10.31	±0.03	−814.76	±0.20
	7200	7.29	0.0000	0.1633	0.4620	−10.29		−814.64	

[a] Bulk composition before dissolution; [b]Bulk composition after 300 d of dissolution;

[c] IAP estimated for the bulk composition after 300 d of dissolution

Lippmann diagram for the nonideal $(Ca,Mn)CO_3$ solid solutions

Regarding the $(Ca,Mn)CO_3$-H_2O SS-AS system, the extent of nonideality and the stability field have been unequivocally established [2]. Several works reported componential ranges from the total miscibility between $CaCO_3$ and $MnCO_3$ to restricted solid solubilities with diverse ranges of miscibility gaps [57, 58]. $CaCO_3$ and $MnCO_3$ are suggested to form a complete series, but many of the intermediate $Mn_xCa_{1-x}CO_3$ compositions are metastable or unstable under ambient conditions [4]. Therefore, the $(Ca,Mn)CO_3$ solid solution is accepted to be nonideal and incomplete at 25 °C; however, it is frequently considered regular. Thus, the estimated values of a_0 found in the literature for this solid solution differ enormously. For example, a theoretically derived $a_0 = +3.23$ (25 °C) was proposed [10], while $a_0 = -1 \pm 3$ at 20 °C was calculated from experimental solubility data [4]. A negative value of a_0 (−3.5 at 5 °C) was also estimated from observations on natural phase relations in marine anoxic sediments [18]. The a_0 parameter was calculated from the miscibility gap [15] to be $a_0 < 2$ at 25 °C [16]. Experimental studies under ambient conditions [5] and high temperatures [59] have shown that a regular

model was probably insufficient to strictly describe thermodynamic equilibrium in this system. The two-parameter Guggenheim expansion equations ("subregular" models) were effectively applied to fit the experimental solubilities of (Sr,Ca)CO_3-H_2O, (Ba,Sr)CO_3-H_2O, and (Ca,Mg)CO_3-H_2O systems [16]. Therefore, in the absence of more precise data, the $(Ca_{1-x}Mn_x)CO_3$ solid solutions were assumed to be subregular, and the two Guggenheim coefficients a_0 and a_1 were calculated in this work.

The solid activity coefficients of $CaCO_3$ (γ_{Ca}) and $MnCO_3$ (γ_{Mn}) in terms of solid components (1−x, x) can be estimated by the Redlich and Kister equations [50, 54, 60], which are expressed as:

$$\ln\gamma_{Ca} = (1-x)^2[a_0 - a_1(3x-(1-x)) + \ldots] \quad (16)$$

$$\ln\gamma_{Mn} = x^2[a_0 - a_1(3(1-x)-x) + \ldots] \quad (17)$$

where 1−x and x are the molar ratios (X_{Ca} and X_{Mn}) of $CaCO_3$ and $MnCO_3$ in the $(Ca_{1-x}Mn_x)CO_3$ solid solutions, respectively.

When the stoichiometric saturation state was reached during dissolution, the excess free energy of mixing for the $(B_xC_{1-x})A$ solid solutions (G^E) can be estimated with the following:

$$G^E = RT[\ln K_{SS} - x(\ln K_{CA} + \ln x) - (1-x)(\ln K_{BA} + \ln(1-x))] \quad (18)$$

where K_{SS} is the stoichiometric saturation constant and K_{CA} and K_{BA} are the solubility products of CA and BA, respectively [34, 50]. The Guggenheim expansion equation for G^E is:

$$G^E = x(1-x)\,RT\,[a_0 + a_1(x-(1-x)) + a_2(x-(1-x))^2\ldots] \quad (19)$$

where a_0, a_1 and a_2 are dimensionless Guggenheim coefficients that usually express the excess free energy of solid solutions in terms of their solid components. Combining Eqs. (18) and (19) and rewriting them for the $(Ca_{1-x}Mn_x)CO_3$ solid solutions while using only the coefficients a_0 and a_1 yields:

$$\ln K_{sp} = x(1-x)a_0 + x(1-x)(x-(1-x))a_1 + (1-x)\ln[(1-x)K_{Ca}] + x\ln[xK_{Mn})] \quad (20)$$

When the stoichiometric saturation state was reached during dissolution, a_0 and a_1 can be calculated by:

$$\ln K_{sp} = x(1-x)a_0 + x(1-x)(x-(1-x))a_1 + (1-x)\ln[(1-x)K_{Ca}] + x\ln[xK_{Mn})] \quad (21)$$

The log_IAP values (≈log_K_{sp}) for the final three solutions after 2400–7200 h dissolution in N_2-degassed, air-saturated and CO_2-saturated ultrapure waters were plotted versus X_{Mn} of the $(Ca_{1-x}Mn_x)CO_3$ solid solutions in Additional file 1: Appendix S9, showing that the experimental log_K_{sp} values were near and slightly lower than those of an ideal $(Ca_{1-x}Mn_x)CO_3$ solid solution. The K_{sp} values as a function of X_{Mn} could be very well fitted to Eq. (21) with the two-parameter Guggenheim models of $a_0 = 2.96$ and $a_1 = -0.20$, $a_0 = 2.92$ and $a_1 = -0.33$ and $a_0 = 3.28$ and $a_1 = 0.61$, respectively. Moreover, the dimensionless Guggenheim parameters were also estimated based on the miscibility gap mole fractions of $MnCO_3$ ($X_{Mn} = 0.11$ and 0.83) at 25 °C after the powder XRD measurements by using the computer code MBSSAS [61] to be $a_0 = 2.52$ and $a_1 = -0.19$. It is obvious that the estimated Guggenheim parameters in the present work were comparable to $a_0 = +3.23$ [10] and were therefore chosen to construct the Lippmann diagrams of the $(Ca_{1-x}Mn_x)CO_3$ solid solutions.

Solid solution–aqueous solution interaction

The study of the precipitation behavior in the (Ca,Mn)CO_3-H_2O system at 25 °C was stated in the literature as being quite problematic [2, 11]. The main reason was that several authors report different values for the solubility product of rhodochrosite (log_K_{MnCO3}) that vary between −9.47 and −12.19 [5, 44]. As a result, there existed a significant discrepancy concerning the calculation of the *solidus* and *solutus* curves [2]. Figure 9a illustrates the Lippmann diagrams of the $(Ca_{1-x}Mn_x)CO_3$ solid solutions at 25 °C, computed with the subregular solid solution ($a_0 = 2.97$ and $a_1 = -0.27$) and the calcite and rhodochrosite endmembers from the present study (log_$K_{CaCO3} = -8.44$ and log_$K_{MnCO3} = -10.26$, respectively). Along with the *solutus* and *solidus* curves, the stoichiometric saturation curves of pure $CaCO_3$ ($X_{Mn} = 0$), the $(Ca_{1-x}Mn_x)CO_3$ solid solutions ($X_{Mn} = 0.21$, 0.42, 0.61 and 0.82) and pure $MnCO_3$ ($X_{Mn} = 1$) were also plotted in the Lippmann diagram, which was characterized by the peritectic point at $X_{Mn^{2+},aq} = 0.00744$. At this point, the aqueous component was in equilibrium with two solid phases ($X_{Mn} = 0.04$ and 0.57) at the same time, which defined the two extremes of the miscibility gap [2].

Additionally, the data of this work were also plotted as $(\{Ca^{2+}\}+\{Mn^{2+}\})\{CO_3^{2-}\}$ versus $X_{Mn^{2+},aq}$ (Fig. 9). An increase in the released Ca^{2+} concentration and the highest Mn^{2+} concentration for the solids were generally viewed in the dissolution progress [4]. The experimental data points indicated that the $(Ca_{1-x}Mn_x)CO_3$

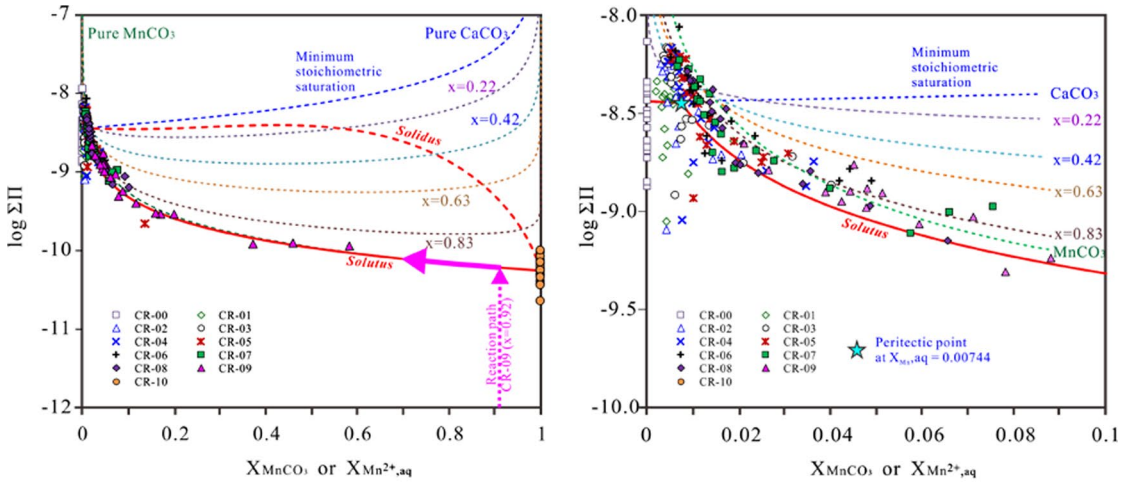

(a) Dissolution in air-saturated water at 25°C; log K_{MnCO3}=-10.26, log K_{CaCO3}=-8.44; a_0=2.92, a_1=-0.33)

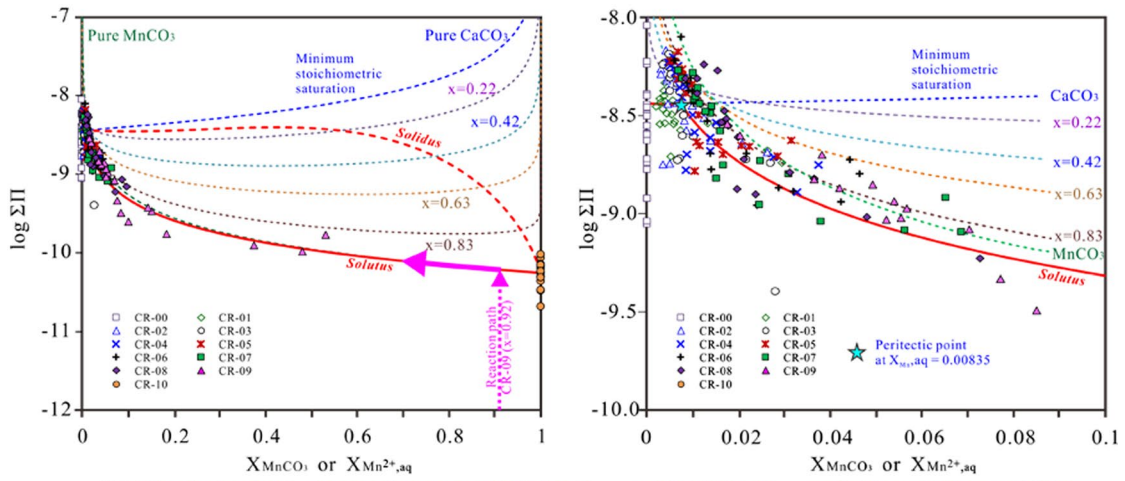

(b) Dissolution in N_2-degassed water at 25°C; log K_{MnCO3}=-10.25, log K_{CaCO3}=-8.46; a_0=2.96, a_1=-0.20)

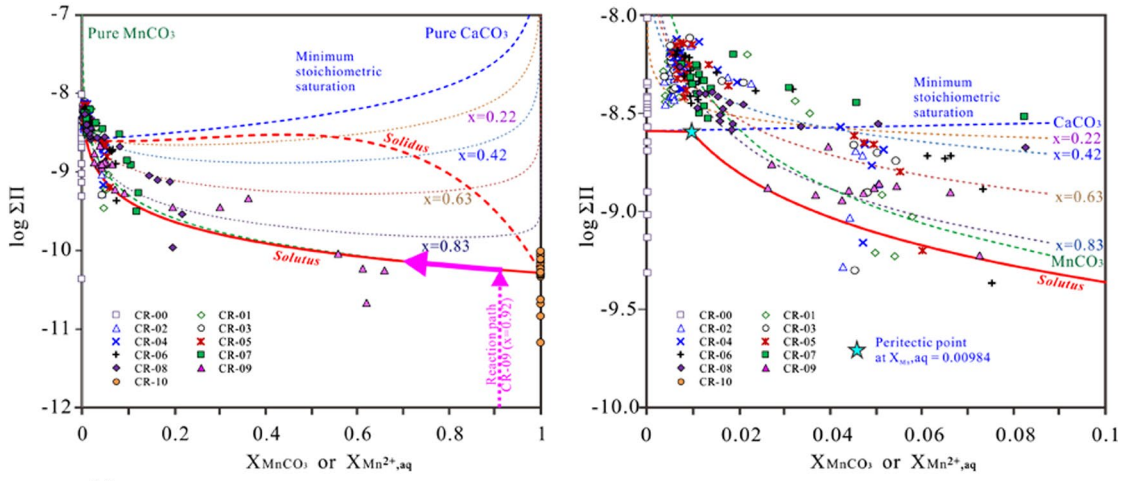

(c) Dissolution in CO_2-saturated water at 25°C; log K_{MnCO3}=-10.28, log K_{CaCO3}=-8.59; a_0=3.28, a_1=-0.61)

Fig. 9 Lippmann diagram of the nonideal $(Ca_{1-x}Mn_x)CO_3$ solid solutions together with the plot of some stoichiometric saturation curves and the experimental data

solid solutions dissolved incongruently and moved progressively up to the *solutus* curve and then along the *solutus* curve and/or the saturation curve of pure $MnCO_3$ from right to left. The aqueous Mn-poor solutions were finally in equilibrium with the $MnCO_3$-rich solids. Because the dissolution of the $(Ca_{1-x}Mn_x)CO_3$ solid solutions was superimposed with the formation of new solid phases with a larger X_{Mn} than the initial solids, the overall dissolution became progressively incongruent for the solid samples (CR-01–CR-09), as reported for $Ca_{0.75}Mn_{0.25}CO_3$ and $Ca_{0.25}Mn_{0.75}CO_3$ [4]. The congruent dissolution part for the solids (CR-01–CR-09) was not detected, most likely due to the very high effective surface of the initial solids that caused quick dissolution and acted as the seeds for forming new solid phases [4]. Generally, the saturation curve for $MnCO_3$ and the *solutus* curve for the $(Ca_{1-x}Mn_x)CO_3$ solid solutions were progressively approached and exceeded during the SS-AS interaction (Fig. 9). The saturation indexes (SI) for rhodochrosite [$MnCO_3$] increased as X_{Mn} increased, and the aqueous solutions were saturated or oversaturated with rhodochrosite [$MnCO_3$] at the end of dissolution at $X_{Mn} > 0.5$ (CR-05–CR-10). The aqueous solutions were finally slightly oversaturated with calcite [$CaCO_3$], with the exception of CR-09 ($X_{Mn} = 0.92$). The highest SI value with respect to calcite [$CaCO_3$] was observed at $X_{Mn} = 0.63$ (CR-06) and then decreased as X_{Mn} decreased or increased (Additional file 1: Appendix S10). These results provide deeper insight into the mechanisms of the geochemical cycle of manganese in the environment.

Conclusions

The crystal morphologies of synthesized $(Ca_{1-x}Mn_x)CO_3$ solid solutions varied from blocky spherical crystal aggregates to smaller spheres following an increasing incorporation of Mn in the solids. The crystals grown from starting aqueous solutions with almost equal concentrations of Mn^{2+} and Ca^{2+} exhibited double peaks that corresponded to the reflections of calcite and rhodochrosite peaks in the XRD patterns and showed clear oscillatory concentric zoning, indicating core-to-rim compositional and crystalline heterogeneities in the solids. The central part of the crystal was always relatively rich in Mn. Surrounding this core were successive Ca-rich and Mn-rich rings.

Regarding the dissolution of the $(Ca_{1-x}Mn_x)CO_3$ solid solutions in N_2-degassed ultrapure water and air-saturated water, the aqueous Ca and $HCO_3 + CO_3$ concentrations increased up to their highest values after 1240–2400 h. The aqueous Mn concentrations and the aqueous Mn/(Ca + Mn) mole ratios increased up to the highest value after 6–12 h of dissolution and then decreased gradually to a steady state. Regarding dissolution in CO_2-saturated water, the aqueous Ca and Mn concentrations reached maximum values within 1 h and then decreased to the steady state. The aqueous pH and Mn concentrations increased with the increasing X_{Mn} of the $(Ca_{1-x}Mn_x)CO_3$ solid solutions, while the aqueous Ca and $HCO_3 + CO_3$ concentrations showed the highest values at $X_{Mn} = 0.53–0.63$.

The average log_IAP values at the final steady state of dissolution ($\approx \log\_K_{sp}$) and the ΔG_f° values were estimated to be $-8.44 \sim -8.59$ and $-1129.63 \sim -1130.48$ kJ/mol, respectively, for calcite [$CaCO_3$] and $-10.25 \sim -10.28$ and $-814.39 \sim -814.59$ kJ/mol for rhodochrosite [$MnCO_3$], respectively. As X_{Mn} increased, the log_IAP values almost linearly decreased.

The plotting of the experimental data as Lippmann diagrams for the subregular $(Ca_{1-x}Mn_x)CO_3$ solid solutions indicated that the solids dissolved incongruently and moved progressively up to the *solutus* curve and then along the *solutus* curve and/or the saturation curve of pure $MnCO_3$ from right to left. The microcrystalline cores of the spherical crystal aggregates were preferentially dissolved to form cavities while simultaneously precipitating Mn-rich hexagonal prisms.

Abbreviations

ICP-OES: Inductively Coupled Plasma-Optical Emission Spectrometry; XRD: X-ray Diffraction; ICDD: International Center for Diffraction Data; FE-SEM: Field Emission Scanning Electron Microscopy; BSEI: Backscattered Electron Imaging; PET: Polyethylene Terephthalate; IAP: Ion Activity Product; SS-AS: Solid Solution–Aqueous Solution.

Supplementary Information

The online version contains supplementary material available at https://doi.org/10.1186/s12932-021-00075-1.

Additional file 1: Appendix S1. Major speciation reactions involved in the PHREEQC calculation. **Appendix S2-A.** Position variation of the strongest peak (104) with X_{Mn} of the $(Ca_{1-x}Mn_x)CO_3$ solid solutions. **Appendix S2-B.** Diffraction patterns of the $(Ca_{1-x}Mn_x)CO_3$ solid solutions after dissolution (a) in N_2-degassed water and (b) in CO_2-saturated water for 300 d. **Appendix S3-A.** SEM images of the $(Ca_{1-x}Mn_x)CO_3$ solid solutions after dissolution in air-saturated water for 300 d. **Appendix S3-B.** SEM images of the $(Ca_{1-x}Mn_x)CO_3$ solid solutions after dissolution in N_2-degassed water for 300 d. **Appendix S3-C.** SEM images of the $(Ca_{1-x}Mn_x)CO_3$ solid solutions after dissolution in CO_2-saturated water for 300 d. **Appendix S4.** BSE images of the equatorial sections and the corresponding compositional profiles along the A-B line of the (a) $(Ca_{0.68}Mn_{0.32})CO_3$ (CR-03) and (b) $(Ca_{0.48}Mn_{0.52})CO_3$ (CR-05) solids after dissolution in air-saturated water for 300 d. **Appendix S5.** BSE images of the equatorial sections and EDS analyses of the $(Ca_{0.68}Mn_{0.32})CO_3$ (CR-03) solid before and after dissolution in air-saturated water for 300 d to show that the microcrystalline sphere cores were preferentially dissolved to form hollows and Mn-rich hexagonal prisms. **Appendix S6.** Variation in the aqueous Mn/(Ca + Mn) mole ratios during the dissolution of the $(Ca_{1-x}Mn_x)CO_3$ solid solutions. **Appendix S7.** XPS patterns of the $(Ca_{1-x}Mn_x)CO_3$ solid solutions (a) before and (b) after dissolution in air-saturated water for 300 d. **Appendix S8.** Dependence of the aqueous components at the experimental end (300 d) on the X_{Mn} of $(Ca_{1-x}Mn_x)CO_3$. **Appendix S9.** Estimation of the Guggenheim coefficients for the nonideal $(Ca_{1-x}Mn_x)CO_3$ solid solutions. **Appendix S10.** Saturation indexes for calcite and rhodochrosite during the dissolution of the $(Ca_{1-x}Mn_x)CO_3$ solid solutions.

Acknowledgements
The manuscript was greatly improved from the insightful comments by Prof. Dr. Jeremy Fein and two anonymous reviewers. The authors are grateful for the financial support from the National Natural Science Foundation of China and the Science & Technology Planning Projects of Guangxi.

Authors' contributions
YZ and ZZ initiated the arrangement of the experiment and drafted the manuscript. NM, PN, HY, XW and LZ carried out most of the experiments and the XRD, FT-IR and FE-SEM analyses. HD and ST interpretated the data. All authors read and approved the final manuscript.

Funding
The present research was funded by the National Natural Science Foundation of China (42063003 and 41763012) and the Science & Technology Planning Projects of Guangxi (2018GXNSFAA050044 and GuiKe-AD18126018).

Availability of data and materials
The datasets used for this manuscript are displayed in the figures in the manuscript and the additional file. The data in tabulated form are available upon request.

Declarations

Competing interests
The authors declare that they have no competing interests.

Author details
[1]College of Environmental Science and Engineering, Guilin University of Technology, Guilin 541004, China. [2]Guangxi Key Laboratory of Environmental Pollution Control Theory and Technology, Guilin University of Technology, Guilin 541004, China. [3]Collaborative Innovation Center for Water Pollution Control and Water Safety in Karst Area, Guilin University of Technology, Guilin 541004, China.

Received: 28 March 2021 Accepted: 21 May 2021
Published online: 26 May 2021

References

1. Crossgrove J, Zheng W (2004) Manganese toxicity upon overexposure. NMR Biomed 17:544–553
2. Katsikopoulos D, Fernández-González Á, Prieto M (2009) Crystallization behaviour of the (Mn, Ca)C_O3 solid solution in silica gel: nucleation, growth and zoning phenomena. Mineral Mag 73:269–284
3. Sternbeck J (1996) Manganese cycling in a eutrophic lake—rates and pathways. Aquat Geochem 1:399–426
4. Böttcher ME (1997) Experimental dissolution of $CaCO_3$-$MnCO_3$ solid solutions in CO_2-H_2O solutions at 20°C: I Synthetic low-temperature carbonates. Solid State Ionics 101–103:1263–1266
5. McBeath MK, Rock PA, Casey WH, Mandell GK (1998) Gibbs energies of formation of metal-carbonate solid solutions: part 3. The $Ca_xMn_{1-x}CO_3$ system at 298 K and 1 bar. Geochim Cosmochim Acta 62:2799–2808
6. Mucci A (2004) The behavior of mixed Ca-Mn carbonates in water and seawater: controls of manganese concentrations in marine porewaters. Aquat Geochem 10:139–169
7. Bamforth SM, Manning DAC, Singleton I, Younger PL, Johnson KL (2006) Manganese removal from mine waters-investigating the occurrence and importance of manganese carbonates. Appl Geochem 21:1274–1287
8. Wang Q, Grau-Crespo R, de Leeuw NH (2011) Mixing thermodynamics of the calcite-structured (Mn, Ca)C_O3 solid solution: A computer simulation study. J Phys Chem B 115:13854–13861
9. Pingitore NE Jr, Eastman MP, Sandidge M, Oden K, Freiha B (1988) The coprecipitation of manganese (II) with calcite: an experimental study. Mar Chem 25:107–120
10. Lippmann F (1980) Phase diagrams depicting the aqueous solubility of binary mineral systems. N Jahrb Mineral Abh 139:1–25
11. Astilleros JM, Pina CM, Fernndez-Daz L, Putnis A (2002) Molecular-scale surface processes during the growth of calcite in the presence of manganese. Geochim Cosmochim Acta 66:3177–3189
12. Kulik DA, Kersten M, Heiser U, Neumann T (2000) Application of Gibbs energy minimization to model early-diagenetic solid-solution aqueous-solution equilibria involving authigenic rhodochrosites in anoxic Baltic Sea sediments. Aquatic Geochem 6:147–199
13. Böttcher ME (1998) Manganese(II) partitioning during experimental precipitation of rhodochrosite–calcite solid solutions from aqueous solutions. Mar Chem 62:287–297
14. Garrels RM, Thompson ME, Siever R (1960) Stability of some carbonates at 25°C and one atmosphere total pressure. Amer J Sci 258:402–418
15. Palache C, Berman H, Frondel C (1951) Dana's system of mineralogy. Wiley, New York
16. Glynn PD (1990) Modeling solid-solution reactions in low-temperature aqueous systems, in Melchior, DC and Bassett, RL, eds, Chemical modeling in aqueous systems II: Am Chem Soc Symposium Series, 416, pp. 74-86
17. Böttcher ME (1997) The transformation of aragonite to $Mn_xCa_{(1-x)}CO_3$ solid-solutions at 20°C: an experimental study. Mar Chem 57:97–106
18. Jakobsen R, Postma D (1989) Formation and solid solution behavior of calcian-rhodochrosites in marine muds of the Baltic deeps. Geochim Cosmochim Acta 53:2639–2648
19. Böttcher ME (2006) The rhodochrosite-calcite solid-solution aqueous-solution system at low temperatures. Geophys Res Abstracts 8:10034
20. Zhang X, Wu S, Chen F (2018) Nano precipitates formed during the dissolution of calcite incorporated with Cu and Mn. Minerals 8(484):1–10
21. Parkhurst DL, Appelo CAJ (2013) Description of input and examples for PHREEQC version 3, A computer program for speciation, batch-reaction, one-dimensional transport, and inverse geochemical calculations. US Geological Survey Techniques and Methods, book 6, chap A43, pp. 497
22. Mucci A (1991) The solubility and free energy of formation of natural kutnahorite. Can Mineral 29:113–121
23. Fernández-Díaz L, Astilleros JM, Pina CM (2006) The morphology of calcite crystals grown in a porous medium doped with divalent cations. Chem Geol 225:314–321
24. Putnis A, Prieto M, Fernández-González L (1995) Fluid supersaturation and crystallization in porous media. Geol Mag 132:1–13
25. Prieto M, Fernández-González A, Putnis A, Fernández-Díaz L (1997) Nucleation, growth, and zoning phenomena in crystallizing (Ba, Sr)CO3, Ba(SO4, CrO4), (Ba, Sr)SO4, and (Cd, Ca)CO3 solid solutions from aqueous solutions. Geochim Cosmochim Acta 61:3383–3397
26. Andara AJ, Heasman DM, Fernández-González Á, Prieto M (2005) Characterization and crystallization of Ba(SO_4, Se_O4) solid solution. Cryst Growth Des 5:1371–1378
27. Fernández-González A, Prieto M, Putnis A, López-Andrés S (1999) Concentric zoning patterns in crystallizing (Cd, Ca)C_O3 solid solutions from aqueous solutions. Mineral Mag 63:331–343
28. Fernández-González A, Pedreira VB, Prieto M (2008) Crystallization of zoned (Ba, Pb)S_O4 single crystals from aqueous solution in silica gel. J Cryst Growth 310:4616–4622
29. Xu M, Riechers SL, Ilton ES, Du Y, Kovarik L, Varga T et al (2017) Manganese-calcium intermixing facilitates heteroepitaxial growth at the (1014) calcite-water interface. Chem Geol 470:152–163
30. Lea AS, Hurt TT, El-Azab A, Amonette JE, Baer DR (2003) Heteroepitaxial growth of a manganese carbonate secondary nano-phase on the (1014) surface of calcite in solution. Surf Sci 524:63–77
31. Pérez-Garrido C, Astilleros JM, Fernández-Díaz L, Prieto M (2009) In situ AFM study of the interaction between calcite 1014 surfaces and supersaturated Mn2+-CO32- aqueous solutions. J Cryst Growth 311:4730–4739
32. Alkattan M, Oelkers EH, Dandurand J-L, Schott J (1998) An experimental study of calcite and limestone dissolution rates as a function of pH from -1 to 3 and temperature from 25 to 80°C. Chem Geol 151:199–214
33. Putnis CV, Ruiz-Agudo E, Hövelmann J (2014) Coupled fluctuations in element release during dolomite dissolution. Mineral Mag 78:1355–1362
34. Baron D, Palmer CD (2002) Solid-solution aqueous-solution interactions between jarosite and its chromate analog. Geochim Cosmochim Acta 66:2841–2853
35. Stumm W, Morgan JJ (1996) Aquatic chemistry, chemical equilibria and rates in natural waters, 3rd edn. Wiley, New York

36. Allison JD, Brown DS, Novo-Gradac KJ (1991) MINTEQA2/PRODEFA2, A geochemical assessment model for environmental systems: Version 3.0 user's manual. Environmental Research Laboratory, Office of Research and Development, US Environmental Protection Agency, Athens, Georgia, United States, pp. 106
37. Plummer L, Busenberg E (1982) The solubilities of calcite, aragonite, and vaterite in carbon dioxide water solutions between 0 and 90℃, and an evaluation of the aqueous model for the system calcium carbonate-carbon dioxide-water. Geochim Cosmochim Acta 46:1011–1040
38. Jensen DL, Boddum JK, Tjell JC, Christensen TH (2002) The solubility of rhodochrosite ($MnCO_3$) and siderite ($FeCO_3$) in anaerobic aquatic environments. Appl Geochem 17:503–511
39. Latimer WM (1952) The oxidation states of the elements and their potentials in aqueous solutions, 2nd edn. Prentice-Hall, New Jersey
40. Morgan JJ (1967) Chemical equilibria and kinetic properties of manganese in natural waters. In: Hunter JV (ed) Principles and applications of water chemistry. Wiley, New York, pp 561–624
41. Johnson KS (1982) Solubility of rhodochrosite ($MnCO_3$) in water and seawater. Geochim Cosmochim Acta 46:1805–1809
42. Wagman DD, William HE, Parker VB, Handhalow R, Schumm I, Bailey SM et al (1982) The NBS tables of chemical thermodynamic properties: Selected values for inorganic and C1 and C2 organic substances in SI units. J Phys Chem Ref Data 11(Suppl):2
43. Néher-Neumann E (1994) Studies on metal-carbonate equilibria 26, The hydrogen carbonate complex of Mn(II) in acid solutions and 3M (Na) ClO_4 ionic medium at 25°C, determination of the solubility product of $MnCO_3$(s). Acta Chim Scand 48:393–398
44. Wolfram O, Krupp RE (1996) Hydrothermal solubility of rhodochrosite, Mn(II) speciation, and equilibrium constants. Geochim Cosmochim Acta 60:3983–3994
45. Robie RA (1966) Handbook of physical constants: thermodynamic properties of minerals. GSA Mem 97:437
46. Robie RA, Hemingwa BS, Fisher JR (1978) Thermodynamic properties of minerals and related substances at 298.15 K and 1 bar pressure and at higher temperatures. USGS Bull 1452
47. Boynton WV (1971) An investigation of the thermodynamics of calcite-rhodochrosite solid solutions. PhD Thesis, Carnegie-Mellon University
48. Luo Y, Millero FJ (2003) Solubility of rhodochrosite ($MnCO_3$) in NaCl solutions. J Sol Chem 32:405–416
49. Oelkers EH, Benezeth P, Pokrovski GS (2009) Thermodynamic databases for water rock interaction. Rev Min Geochem 70:1–46
50. Glynn PD, Reardon EJ (1990) Solid-solution aqueous-solution equilibria: thermodynamic theory and representation. Amer J Sci 290:164–201
51. Glynn PD, Reardon EJ, Plummer LN, Busenberg E (1990) Reaction paths and equilibrium end-points in solid-solution aqueous-solution systems. Geochim Cosmochim Acta 54:267–282
52. Monnin C (1999) A thermodynamic model for the solubility of barite and celestite in electrolyte solutions and seawater to 200°C and to 1kbar. Chem Geol 153:187–209
53. Gamsjäger H, Königsberger E, Preis W (2000) Lippmann diagrams: theory and application to carbonate systems. Aquat Geochem 6:119–132
54. Prieto M (2009) Thermodynamics of solid solution aqueous solution systems. Rev Mineral Geochem 70:47–85
55. Katsikopoulos D, Fernández-González Á, Prieto M (2009) Precipitation and mixing properties of the "disordered" (Mn, Ca)C_O3 solid solution. Geochim Cosmochim Acta 73:6147–6161
56. Böttcher ME, Dietzel M (2010) Metal-ion partitioning during low-temperature precipitation and dissolution of anhydrous carbonates and sulphates. EMU Notes Mineral 10:139–187
57. Goldsmith JR, Graf DL (1957) The system CaO-MnO-CO_2: solid solution and decomposition reactions. Geochim Cosmochim Acta 11:301–334
58. Fubini B, Stone FS (1983) Physico-chemical properties of $MnCO_3$-$CaCO_3$ and MnO-CaO solid solution. J Chem Soc Faraday T 79:1215–1227
59. Capobianco C, Navrotsky A (1987) Solid-solution thermodynamics in $CaCO_3$-$MnCO_3$. Am Mineral 72:312–318
60. Redlich O, Kister AT (1948) Algebraic representation of thermodynamic properties and the classification of solutions. Ind Eng Chem 40:345–348
61. Glynn PD (1991) MBSSAS: A code for the computation of Margules parameters and equilibrium relations in binary solid-solution aqueous-solution systems. Comput Geosci 17:907–966

Publisher's Note